aerospace

MDPI

Article

Reduction in Aeolian Tone for a Laminar Flow Past a D-Shaped Cylinder Using Arc-Shaped Splitter Plates

Bo Luo [1,2], Xiangyi Chen [2], Wuli Chu [3], Kyle Jiang [2,4,*], Qiao Chen [2] and Guoliang Qin [1]

[1] School of Energy and Power Engineering, Xi'an Jiaotong University, Xi'an 710049, China; lbtoday@outlook.com (B.L.)
[2] Yangtze Delta Region Institute of Tsinghua University, Zhejiang, Jiaxing 314006, China
[3] School of Power and Energy, Northwestern Polytechnical University, Xi'an 710129, China
[4] School of Mechanical Engineering, University of Birmingham, Birmingham B15 2TT, UK
* Correspondence: k.jiang@bham.ac.uk

Abstract

This investigation is to address the aerodynamic noise generated from laminar flow over a D-shaped cylinder at a low Reynolds number (Re). Proposed is a novel assembly of arc-shaped splitter plates to effectively reduce the aeolian tone for the D-shaped cylinder. The two-dimensional flow field is simulated at an Re of 160 to investigate the mechanism of reducing the sound of the arc-shaped plates. The radiated sound has been predicted by Ffowcs Williams and Hawkings (FW-H) acoustic analogy. To verify calculations, the predicted results of a circular cylinder have been compared with the data in the literature. The results reveal that the introduction of the arc plates decreases the lift and drag fluctuations as well as the vortex shedding frequency in comparison with the no-arc plate case. The pressure and velocity fluctuations in the wake zone are reduced by the arc plates due to vortex shedding suppression. The application of the arc plates shows an effective control of sound, leading to a maximum reduction in sound pressure level (SPL) by almost 34 dB.

Keywords: aeroacoustics; D-shaped cylinder; reduction in sound; splitter plate; vortex shedding suppression

1. Introduction

The aerodynamic noise emitted from bluff bodies is a practically important problem in many engineering applications such as aircraft, high-speed trains, automobiles, and so on [1,2]. The periodic vortex shedding from bluff bodies leads to a strong aeolian tone. This annoying noise in flows can be suppressed by controlling vortex shedding. The reduction in aeolian tone from bluff bodies has been a subject of interest in the fields of aeronautics and astronautics. Thus, efficient techniques for suppressing vortex shedding and sound have received much attention [3–5].

Passive flow control is an attractive method to suppress vortex shedding and mitigate the aerodynamic noise for bluff bodies, such as adding grooves by Fujisawa et al. [6], inserting a downstream wedge by Samion et al. [7], and using splitter plates by Dai et al. [8]. Among these passive methods, using splitter plates is an interesting and cost-effective approach to suppressing vortex shedding and aerodynamic noise [9–13]. Ali et al. [14] examined the noise from a square cylinder with a splitter plate for Re = 150 in two-dimensional simulations. Their results showed that the noise sources for the square cylinder were dominated by lift fluctuations, and the sound levels were decreased when the length of the flat plate was less than the cylinder diameter (D). In another study, Ali et al. [15]

Check for updates

Academic Editors: Firoz Alam, Yingai Jin and Xingjun Hu

Received: 7 January 2026
Revised: 16 March 2026
Accepted: 18 March 2026
Published: 30 March 2026

Copyright: © 2026 by the authors. Licensee MDPI, Basel, Switzerland. This article is an open access article distributed under the terms and conditions of the Creative Commons Attribution (CC BY) license.

numerically investigated the aeolian tone from a square cylinder with a detached flat plate and found that a 6.3 dB reduction was achieved with the length of the plate as 0.26D and its distance as 5.6D downstream of the cylinder. Vortex shedding around a circular cylinder with a splitter plate at Reynolds numbers of 100 and 160 was calculated by You et al. [16] in two-dimensional unsteady calculations. They found that adding the splitter plate had different effects on the sound sources at Re = 100 and at Re = 160. Abbasi et al. [17] conducted a numerical study into investigating the application of a splitter plate to reduce noise from a square cylinder. Their results showed that a splitter plate with its length varying from 0.2 to 2D gave reductions in SPL and mean drag force in comparison with the no-plate case. Numerical calculations for a circular cylinder with a splitter plate have been conducted at an Re of 97,300 by Karthik et al. [18] using large eddy simulation (LES) and FW-H equations to evaluate the aerodynamic and acoustic performance. Their study showed that a reduction in OASPL by 6.41 dB and drag force by 34.62% was obtained by an optimal plate length compared with the unmodified cylinder case. The impact of short splitter plates on the radiated aeolian tone of two side-by-side square cylinders in Re = 1.0–3.3 $\times$ 10^4 was studied by Ressa and Asai [19]. The authors of [19] have shown that the aeolian tone was apparently suppressed by short splitter plates with length less than 0.5D.

However, most of previous studies only focused on either an attached or detached flat plate. There are quite limited studies related to any alternate splitter plate for the control of aerodynamic noise for bluff bodies. In addition, a D-shaped cylinder, made of a semicircular leading edge continuing into a rectangular aft section, is a basic configuration in the industrial field, whereas there are fewer studies about the aerodynamics and sound of a D-shaped cylinder as compared to a circular cylinder [20]. The flow around a D-shaped cylinder has a number of practical applications in the wing mirrors of vehicles, skyscraper structures, abutments, vortex generators of vortex flowmeters, high-speed trains, blunt airfoils, devices such as heat exchangers in the food industry, fibrous processing, the paper industry, etc. [21–23]. For example, a wing mirror of a vehicle can be seen as a D-shaped cylinder. Because of its location on the vehicle, it leads to drag and noise emissions [24,25]. Approximately 10% of the total drag acting on a vehicle is the result of the wing mirrors, with 0.5% of the total projection surface area [26]. Whistle noise from a simplified wing mirror model was experimentally studied by Lee et al. [27] in an anechoic wind tunnel to determine the mechanism, and the high-frequency aeolian tone and its harmonics can be observed. In another study, Yamagata et al. [20] experimentally and numerically investigated the aeolian tone from a D-shaped cylinder for various width-to-height ratios and reported that the aeolian tone and lift fluctuations of the D-shaped cylinders were smaller relative to the circular cylinder. The passive control of the turbulent drag by a small secondary cylinder placed behind a D-shaped cylinder was experimentally investigated by Thiria et al. [28], and a maximum drag reduction of 17.5% can be achieved by the appropriate localization of the smaller cylinder. To the authors' knowledge, there are much fewer investigations into the control method for mitigating the aeolian tone and vortex shedding in a D-shaped cylinder. Therefore, in the present study, a novel assembly of arc-shaped splitter plates, which helps to reduce aerodynamic sound, has been used for a D-shaped cylinder. The flow and sound of a D-shaped cylinder with and without the arc splitter plates are investigated to explore the suppression of vortex shedding and sound.

The objective of this paper is to study the mechanism of mitigating the aeolian tone for a novel assembly of arc-shaped plates behind a D-shaped cylinder. Flow simulations have been conducted using two-dimensional calculations at Re = 160 and a Mach number (Ma) of 0.2. This Reynolds number is chosen because with Re $\leq$ 160, two-dimensional structures are dominant, and the flow dynamics and acoustics can be treated as a two-dimensional

model. At the same time, Re must be large enough for sound generation. Thus, the Re of 160 is chosen to perform the simulations. In what follows, the computational details and validation study are addressed in Section 2. Results and discussion are given in Section 3. Finally, a summary of this study is concluded in Section 4.

2. Computational Methods and Validation

2.1. Governing Equations

The governing equations for an unsteady and compressible flow can be written in the following form.

Continuity equation:

$$\frac{\partial \rho}{\partial t} + \frac{\partial (\rho u)}{\partial x} + \partial \frac{(\rho v)}{\partial y} = 0 \tag{1}$$

Momentum equation in x-direction:

$$\frac{\partial (\rho u)}{\partial t} + \frac{\partial \left(\rho u^2 + p\right)}{\partial x} + \frac{\partial (\rho u v)}{\partial y} = \frac{\partial \tau_{xx}}{\partial x} + \frac{\partial \tau_{xy}}{\partial y} \tag{2}$$

Momentum equation in y-direction:

$$\frac{\partial (\rho v)}{\partial t} + \frac{\partial (\rho u v)}{\partial x} + \frac{\partial \left(\rho v^2 + p\right)}{\partial y} = \frac{\partial \tau_{xy}}{\partial x} + \frac{\partial \tau_{yy}}{\partial y} \tag{3}$$

Energy equation:

$$\frac{\partial (\rho E)}{\partial t} + \frac{\partial (\rho u E + p u)}{\partial x} + \frac{\partial (\rho v E + p v)}{\partial y} = \frac{\partial \left(u \tau_{xx} + v \tau_{xy} - q_x\right)}{\partial x} + \frac{\partial \left(u \tau_{xy} + v \tau_{yy} - q_y\right)}{\partial y} \tag{4}$$

The viscous stresses τ_{xx}, τ_{xy}, τ_{yx}, and τ_{yy} are defined as

$$\tau_{xx} = 2\mu \left[\frac{\partial u}{\partial x} - \frac{1}{3}\left(\frac{\partial u}{\partial x} + \frac{\partial v}{\partial y}\right)\right] \tag{5}$$

$$\tau_{yy} = 2\mu \left[\frac{\partial v}{\partial y} - \frac{1}{3}\left(\frac{\partial u}{\partial x} + \frac{\partial v}{\partial y}\right)\right] \tag{6}$$

$$\tau_{xy} = \tau_{xy} = \mu \left(\frac{\partial u}{\partial y} + \frac{\partial v}{\partial x}\right) \tag{7}$$

The heat fluxes, q_x and q_y, are defined as

$$q_x = -k_t \frac{\partial T}{\partial x} \tag{8}$$

$$q_y = -k_t \frac{\partial T}{\partial y} \tag{9}$$

For a compressible flow, the ideal gas law is defined as

$$p = \rho R T \tag{10}$$

where p is the pressure, ρ is the density, R is the universal gas constant, and T is the temperature.

2.2. Acoustic Predictions

The generated sound is predicted by using the Ffowcs Williams-Hawkings formulations [29], derived as an extension of Lighthill's acoustic analogy [30]. This approach computes the far-field sound based on near-field hydrodynamic data obtained from com-

putational fluid dynamics (CFD) simulations. The FW-H equation is given in the following form:

$$\begin{aligned}\left(\frac{1}{c_0^2}\frac{\partial^2}{\partial t^2}-\nabla^2\right)p(\mathbf{x},t) &= \frac{\partial}{\partial t}\{[\rho_0 v_n+\rho(u_n-v_n)]\delta(f)\}\\ &-\frac{\partial}{\partial x_i}\{[P_{ij}n_j+\rho u_i(u_n-v_n)]\delta(f)\}\\ &+\frac{\partial^2}{\partial x_i\partial x_j}[T_{ij}H(f)]\end{aligned} \tag{11}$$

The three terms represent monopole, dipole, and quadrupole, respectively, in the right side of Equation (11). The monopole source term results from the dilatation of boundaries, sometimes mentioned as thickness noise. The dipole source term is associated with the fluctuating forces on the surface, sometimes mentioned as loading noise. The quadrupole source term physically means unsteadiness inside the fluid represented by the Lighthill tensor.

The sound pressure is given in Equation (12), in which the terms T, L, and Q correspond to the thickness (monopole), loading (dipole), and quadrupole sources, respectively. Detailed mathematical expressions for these components are provided in Equations (13)–(15), respectively [31].

$$p'(\mathbf{x},t) = p'_T(\mathbf{x},t)+p'_L(\mathbf{x},t)+p'_Q(\mathbf{x},t) \tag{12}$$

The monopole sound based on Farassat's formulation 1A is given by:

$$p'_T(\mathbf{x},t)=\frac{1}{4\pi}\left(\int_{f=0}\left[\frac{\rho_0\left(\dot{U}_n+U_{\dot{n}}\right)}{r(1-M_r)^2}\right]_{ret}dS+\int_{f=0}\left[\frac{\rho_0 U_n\left[r\dot{M}_r+a_0\left(M_r-M^2\right)\right]}{r^2(1-M_r)^3}\right]_{ret}dS\right) \tag{13}$$

The dipole sound is given by:

$$p'_L(\mathbf{x},t)=\frac{1}{4\pi}\left(\frac{1}{a_0}\int_{f=0}\left[\frac{\dot{L}_r}{r(1-M_r)^2}\right]_{ret}dS+\int_{f=0}\left[\frac{L_r-L_M}{r^2(1-M_r)^2}\right]_{ret}dS+\frac{1}{a_0}\int_{f=0}\left[\frac{L_r\left[r\dot{M}_r+a_0\left(M_r-M^2\right)\right]}{r^2(1-M_r)^3}\right]_{ret}dS\right) \tag{14}$$

The quadrupole term is given by:

$$p'_Q(\mathbf{x},t)=\frac{1}{4\pi}\left(\left(\frac{\partial^2}{\partial x_i\partial x_j}\right)\int_V\left[\frac{\rho_0 T_{ij}}{(r(1-M_r))}\right]_{ret}dV\right) \tag{15}$$

where $1-M_r$ is the Doppler factor, $r=|\mathbf{x}-\mathbf{y}|$, and the variables are computed in the retarded time $t_{ret}=t-r/c$.

In the present study, the acoustic prediction is conducted using the permeable FW-H equation based on the CFD results of the permeable control surface. The permeable control surface used is $-5\text{D}<x<30\text{D}$ and $-5\text{D}<y<5\text{D}$, where $x=0$ and $y=0$ correspond to the center location of the D-shaped cylinder. The permeable control surface is set to be open downstream, avoiding the generation of spurious waves due to the crossing of the wake through the integration surface. When the thickness and loading terms are computed on the permeable control surface, the acoustic prediction inherently incorporates the quadrupole-induced sound inside the surface. A comprehensive explanation of the acoustic model is presented in the work of Farassat and Brentner [31,32].

2.3. Computational Details

A commercial code STAR-CCM+ version 12.02 is applied for the numerical simulations of a flow field. The two-dimensional, compressible flow is simulated in the laminar regime. Second-order temporal and spatial discretization practices are applied. For the two-dimensional flow calculations, the flow domain is depicted in Figure 1a, where D is

the diameter of the corresponding circular cylinder. To avoid spurious sound due to an active flux at the exit boundary, the outflow boundary is expanded up to 150D [16]. The boundaries of the computational domain are defined as the frees-tream conditions based on the non-reflecting boundary conditions and no-slip walls on all solid surfaces. The time step is determined based on a convective CFL number less than 1. The frequency (f) is normalized by the Strouhal number (St, St= f D/U_∞).

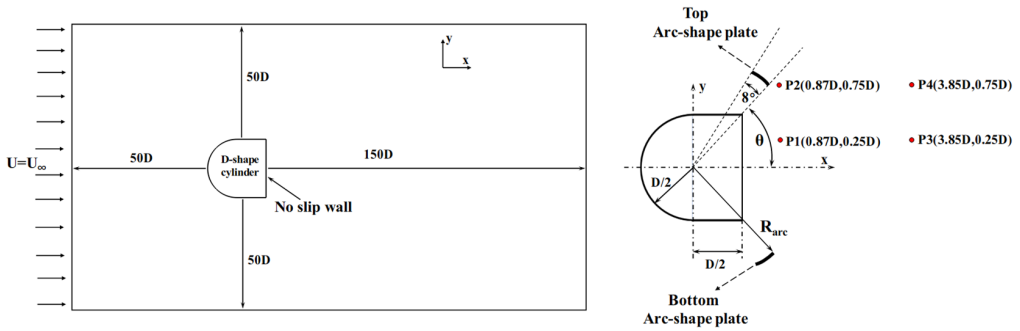

Figure 1. Schematic of the computational domain and the arrangement of arc-shaped splitter plates. (**a**) The computational domain and (**b**) the D-shaped cylinder with the arc plates (not to scale).

To suppress vortex shedding and aeolian tone, the splitter plates with an arc shape are symmetrically located close to the upper and lower sides of the D-shaped cylinder, as illustrated by Figure 1b. The radial distance of each arc plate is represented by R_{arc}, and its angular location from the x-axis is kept at θ = 45°. A constant thickness of 0.005D for the splitter plate is utilized. It should be noted that the probes P1~P4 have been placed in the wake region to investigate pressure fluctuations, as described in the following section. Additionally, the concave wall of the arc plate towards the D-shaped cylinder is described as the inner wall, while the other convex wall is described as the outer wall. Calculations are carried out in different radial distances (R_{arc} = 0.85D, R_{arc} = 1.05D and R_{arc} = 1.2D) and arc angles of the arc-shaped plates (2°, 8° and 14°) in the following part to investigate the effects on flow field and noise.

For the current simulations, polygonal elements are used to discretize the computational domain. The prism layer mesh has been taken with refinement near the cylinder and splitter plate surfaces to adequately resolve the flow details. A wake refinement region extending 30D downstream is employed to adequately capture the vortex shedding dynamics. Based on a mesh independence study conducted for four different grid resolutions in Table 1, a very fine mesh is used consistently for all subsequent simulations.

Table 1. Mesh independence study.

Case	Grid Elements	Mean Drag Coefficient	Strouhal Number
Coarse	23,256	1.333	0.183
Medium	75,424	1.355	0.186
Fine	228,972	1.351	0.186
Very fine	735,758	1.350	0.186

The post-processing stage commences after the flow field reaches a statistically steady or periodic state. Flow fields (vorticity contours and pressure and velocity fluctuations) have been visualized to elucidate the wake topology and flow dynamics, enabling the comparison between the baseline and the configurations with the arc-shaped splitter plates. Quantitative analysis then proceeded with the extraction of force coefficients, where monitors have been created for lift and drag coefficients in time history. Frequency spectral

analysis has been performed by applying Fast Fourier Transform (FFT) with Hanning windowing to the time series of lift and drag coefficients and pressure signals from the probe points placed in the wake, identifying the dominant frequencies and the Strouhal number for each configuration.

The numerical procedure for the acoustic prediction in STAR-CCM+ version 12.02 has been implemented through its integrated FW-H acoustic analogy solver, which operated in a coupled manner with the unsteady flow simulation. For the present study, the On-the-Fly FW-H Model was activated by selecting the "Aeroacoustics" and " Ffowcs Williams-Hawkings Unsteady". The FW-H model requires defining the receiver (virtual microphone) positions in the far field and selecting the source surfaces for acoustic integration. The permeable control surface has been defined as the FW-H acoustic source surface. The FW-H solver then performed a time-domain integration using the source surface data to compute the acoustic pressure at each receiver. Following the simulation, post-processing of acoustic data has been performed using built-in dataset functions. The time-domain sound pressure was transformed to the frequency domain via Fast Fourier Transform (FFT) to obtain frequency information. For the directivity analysis of sound, the root mean square sound pressure at multiple angular positions has been extracted and visualized in polar plots.

2.4. Validation Study

To verify calculations, the predicted results of a circular cylinder have been evaluated against the literature values, as shown in Figure 2. The validation has been carried out for time-averaged drag (*Cd.avg*) and Strouhal number variation with Re. The *Cd.avg* of the present calculations are in good agreement with the literature values for the different Re [33–35]. In the range of the investigated Re, the predicted St corresponding to the vortex shedding frequency increases as the Reynolds number increases. The predicted St at Re = 160 in the present simulation agrees well with data reported by Williamson [36]. This value is slightly lower than the St of vortex shedding frequency reported by Soumya and Prakash [33], as shown in Table 2. Overall, the predicted results in the current computation are in good agreement with the previous data in the literature. Therefore, it is evident that the current numerical algorithm has proven reliable for the calculations.

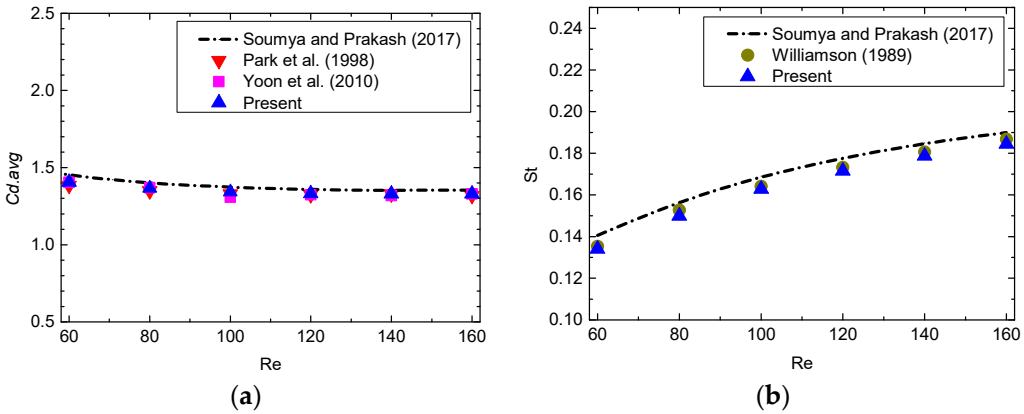

Figure 2. Comparison of the predicted results with the previous data from the literature. (**a**) *Cd.avg* variation with Re [33–35] and (**b**) St variation with Re [33,36].

Table 2. Comparison of flow parameters for circular cylinder case with literature values at Re = 160.

Parameter	Soumya and Prakash (2017) [33]	Present	Relative Error
Cd.avg	1.35	1.313	2.74%
St	0.189	0.186	1.59%

2.5. Theoretical Framework for Noise Reduction Mechanism

For a bluff body like the D-shaped cylinder, the dominant source of aeolian tone is the periodic fluctuating lift and drag forces caused by alternate vortex shedding (Kármán vortex street), as shown in Figure 3a. The symbols ω_z (−) and ω_z (+) in Figure 3 denote the negative and positive vorticity within the shear layers, respectively. The proposed arc-shaped splitter plates function as a passive flow control device targeting the fundamental mechanism. As illustrated in Figure 3b, the amalgamation of the shear layers occurs when these shear layers share the vorticity with the same sign. Conversely, shear layers characterized by the opposite sign of vorticity undergo vorticity cancellation [37,38]. The underlying principle of the arc-shaped splitter plates for mitigating vortex shedding is achieved through flow redirection, wake elongation, and secondary vorticity introduction. The curved splitter plates actively redirect and modify the shear layer trajectories from the D-cylinder, which can disrupt the synchronized, alternate vortex shedding, leading to an acoustically less efficient source. In addition, the splitter plates physically extend the afterbody, increasing the vortex formation length. This elongates the separating shear layers, weakening their interaction and reducing the strength of vortex shedding. Furthermore, the presence of the arc plates themselves generates additional, counter-rotating shear layers. The interaction between these and the shear layers from the D-cylinder can promote the vorticity cancellation process, further dissipating energy in the wake.

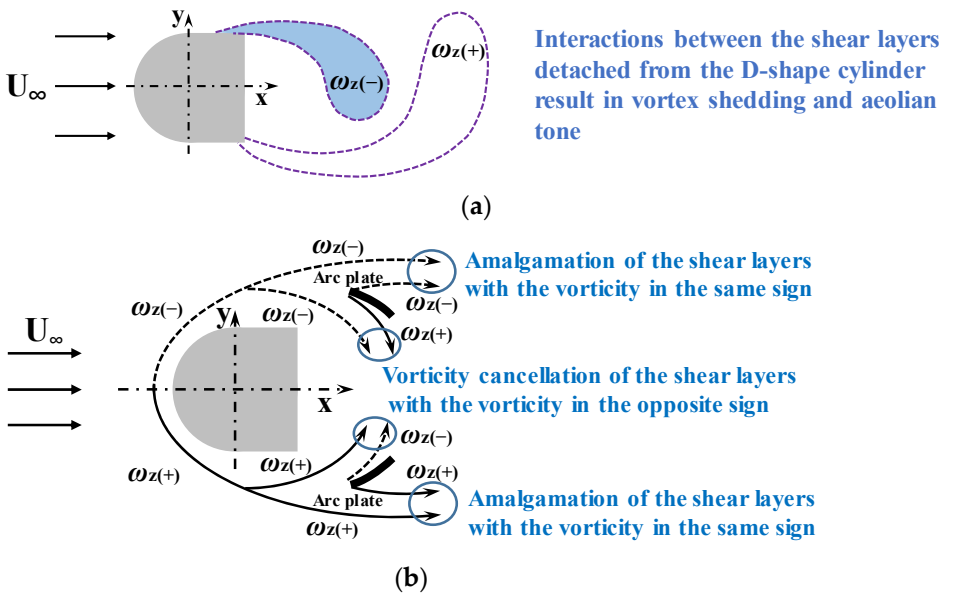

Figure 3. Schematic of the interaction between the separated shear layers. (**a**) The D-shaped cylinder and (**b**) the D-shaped cylinder with the arc plates.

The Strouhal number (St = f D/U_∞) is the key dimensionless parameter linking the vortex shedding frequency (f), the flow velocity (U_∞), and the body's characteristic dimension (D). An effective splitter plate for noise mitigation can suppress the dominant tonal peak at the primary Strouhal frequency and reduce the overall amplitude of the acoustic spectrum. This is achieved by shifting the vortex shedding frequency, typically

through adjustments to the effective wake width or shear-layer convection speed, which alters the Strouhal number and disrupts the vortex shedding. Consequently, the noise reduction manifests as both amplitude suppression and a measurable shift in the dominant frequency peak.

The Reynolds number dictates the flow regime and directly influences noise generation and control mechanisms. At a low Re (laminar regime, as in the present study), vortex shedding is laminar and highly periodic, resulting in a strong, pure tone. The splitter plate's mechanism is primarily the suppression of the laminar vortex street. At a high Re (turbulent regime, for practical relevance), the shear layers separating from the body become turbulent, and vortex shedding, while still periodic, is modulated by turbulent fluctuations. This leads to a tonal peak superimposed on a broadband spectrum. Here, the splitter plates must function in a turbulent environment. While the effectiveness of a passive control device might vary with Re, the mechanistic principle for noise reduction—disrupting large-scale vortex shedding—remains valid.

3. Results and Discussion

3.1. Effects of the Radial Position of the Arc-Shaped Splitter Plates on the Flow and Sound

Figure 4 illustrates the instantaneous contours of vorticity z for the D-shaped cylinder with and without the arc plates. In this subsection, unless otherwise specified, the arc angle of the arc plates is fixed at 8°. In the D-shaped cylinder case, the interaction between the separated shear layers induces Kármán vortex shedding near the D-shaped cylinder. For the cases with arc splitter plates, substantial changes can be found in the flow dynamics in Figure 4. Upon using the arc splitter plates, the shear flows developed from the D-shaped cylinder interact with those from the arc plates and move downstream. A gap between the D-shaped cylinder and the arc plate is a crucial factor since it determines the amount of fluid injected into the gap and the degree of vorticity cancellation [37,38]. For R_{arc} = 0.85D, a small amount of fluid is injected into the gap. Shear layers from the upper side of the D-shaped cylinder and the inner wall of the top arc-shaped plate in the opposite angular rotation undergo vorticity cancellation. A similar process for the lower side of the D-shaped cylinder and the nearby arc plate occurs. In addition, the merged shear layers, from the upper side of D-shaped cylinder − the outer wall of the top arc plate and the lower side of D-shaped cylinder − the outer wall of the bottom arc plate, interact with each other and travel downstream, dictating the formation zone of vortex shedding. For R_{arc} = 1.05D, a larger amount of fluid is injected into the gap compared with R_{arc} = 0.85D, which leads to a considerable degree of vorticity cancellation. The fluid rolls and moves downstream, losing energy as a result of vorticity cancellation [30,31]. The process of vorticity cancellation effectively takes place near the D-shaped cylinder, causing a low-intensity vorticity zone in the wake. Additionally, the merged shear layers become stretched and travel downstream until the generation of periodic vortex shedding in comparison with the no-arc plate case. For a larger radial distance of the arc plates in R_{arc} = 1.2D, almost entire shear layers separated from both the upper and lower sides of D-shaped cylinder are injected into the gap between the arc plates and D-shaped cylinder, which causes vortex shedding once again near the D-shaped cylinder. The implementation of R_{arc} = 1.2D decrease the formation length and raise intensities of the interactions between shear layers in comparison with R_{arc} = 1.05D.

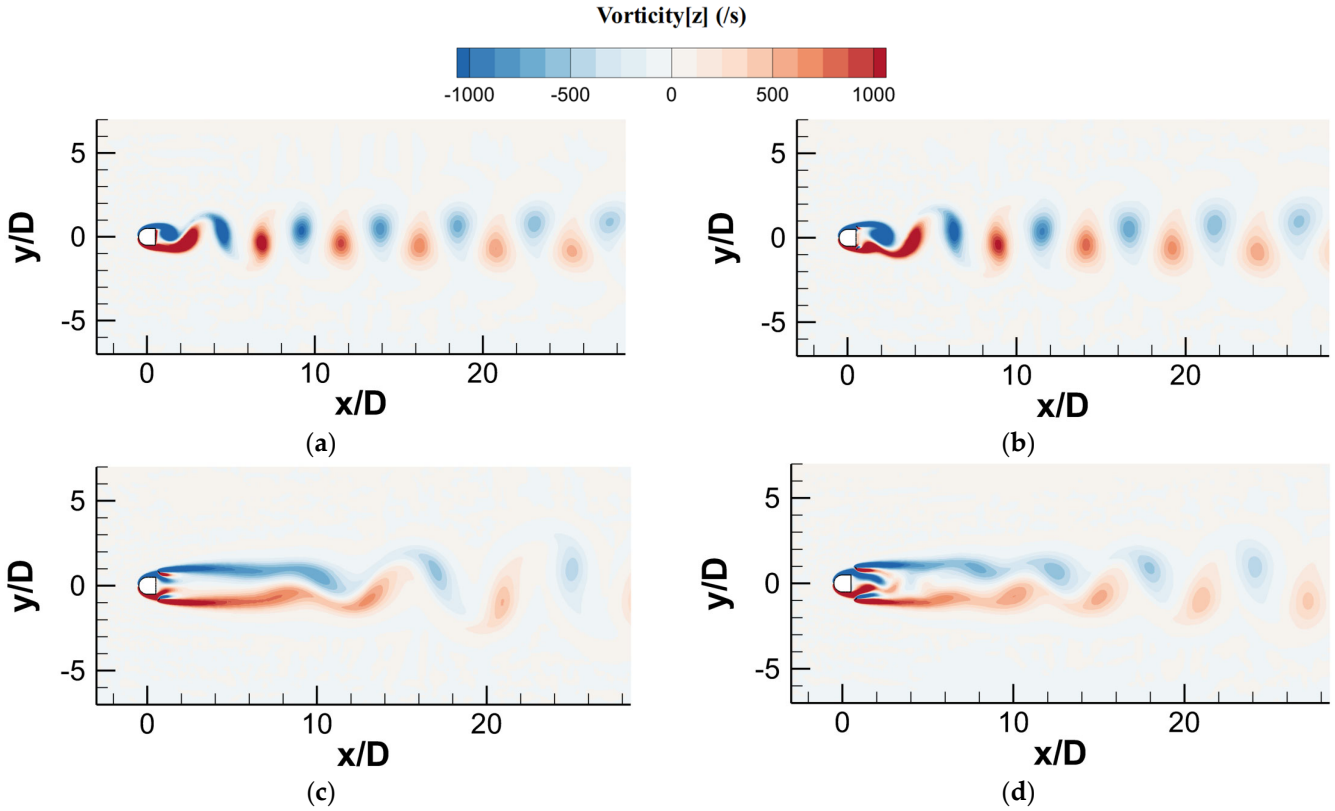

Figure 4. Instantaneous contours of vorticity z for the D-shaped cylinder with and without the arc plates. (**a**) The no-arc plate case, (**b**) R_{arc} = 0.85D, (**c**) R_{arc} = 1.05D, and (**d**) R_{arc} = 1.2D.

Figures 5 and 6 depict the time-trace lift and drag coefficients and the corresponding frequency spectra. The results show that the magnitudes of the lift fluctuations are significantly higher than those of the drag fluctuations in these cases. For the D-shaped cylinder without the arc plates, the amplitude of lift fluctuations in the spectra exhibits a distinct peak with an St around 0.186 in Figure 6a, which corresponds to the Kármán vortex shedding frequency. In the spectra of the drag fluctuations, a peak appears at the harmonics of the vortex shedding frequency around St = 0.37. The interactions between the shear flows detached from the D-shaped cylinder take place near the cylinder surface, resulting in significant amplitudes in fluctuations of lift and drag forces. When the arc plates are introduced, the results show that the magnitudes of the lift and drag fluctuations decrease in intensity, and the peak values occur at a lower St relative to the no-arc plate case. In the R_{arc} = 0.85D case, the magnitudes of lift and drag fluctuations drop in comparison with the no-arc plate case owing to vorticity cancellation. When the arc plates are positioned at R_{arc} = 1.05D, the magnitudes of the lift and drag fluctuations reach the minimum among all the indicated cases. Unlike the D-shaped cylinder without the arc plates, a main peak appears at the vortex shedding frequency of 0.114 for the spectra of fluctuating drag coefficients as a result of the effects of the lift fluctuations together with the significantly reduced drag fluctuations for the R_{arc} = 1.05D case. At the same time, the drag coefficient in R_{arc} = 1.05D is reduced by the arc plates according to Figure 4b, which is usually beneficial to bluff bodies. With further increasing the radial distance to R_{arc} = 1.2D, the magnitudes of lift and drag fluctuations are increased in comparison with the R_{arc} = 1.05D due to vortex shedding once again close to the D-shaped cylinder.

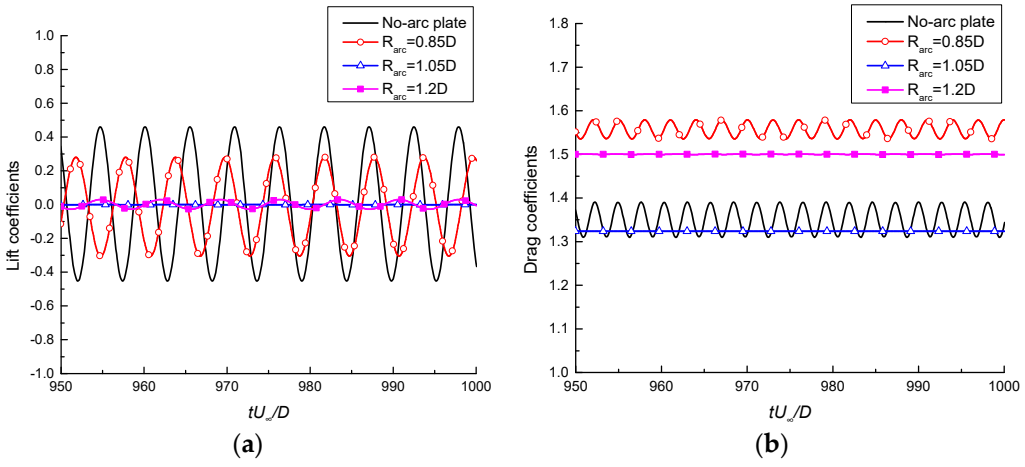

Figure 5. Time histories of lift and drag coefficients for various radial locations. (**a**) Time histories of lift coefficients and (**b**) time histories of drag coefficients.

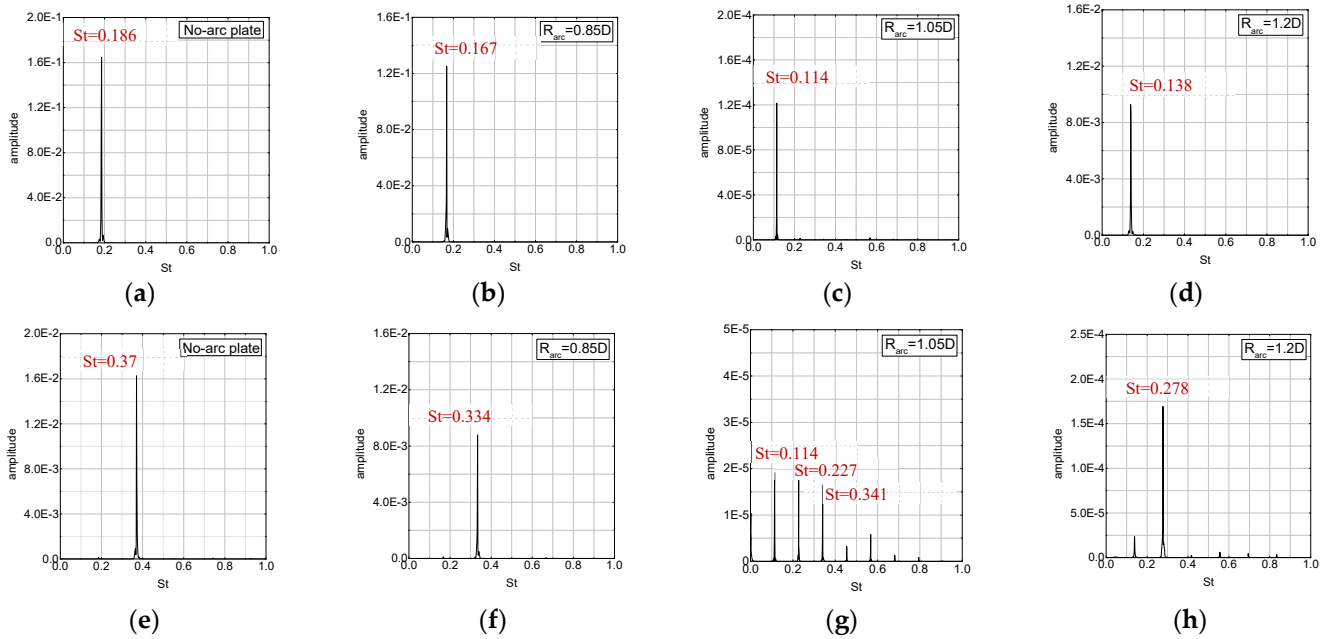

Figure 6. Frequency spectra of lift and drag fluctuations for various radial locations. Spectra of fluctuating lift coefficients for (**a**) the no-arc plate case, (**b**) R_{arc} = 0.85D, (**c**) R_{arc} = 1.05D, and (**d**) R_{arc} = 1.2D. Spectra of fluctuating drag coefficients for (**e**) the no-arc plate case, (**f**) R_{arc} = 0.85D, (**g**) R_{arc} = 1.05D, and (**h**) R_{arc} = 1.2D.

Moreover, for the D-shaped cylinder without the arc plates, the St of vortex shedding is 0.186, and it decreases to 0.167 in the R_{arc} = 0.85D as a result of the diffused separated shear layer. Subsequently, it is further reduced to 0.114 at R_{arc} = 1.05D due to further stretched shear layers and increased formation length. For a larger radial distance of the arc plates at R_{arc} = 1.2D, the vortex shedding frequency is increased to 0.138 due to vortex shedding once again near the D-shaped cylinder and the decreased formation length compared with the R_{arc} = 1.05D case. Obviously, the application of the arc plates suppresses vortex shedding, thereby mitigating the force fluctuations at the D-shaped cylinder surface. Consequently, the lift and drag fluctuations are decreased by the arc splitter plates. Additionally, the separated shear layers become stretched and forced to move downstream, delaying the formation of vortex shedding with the arc plates. Therefore, the Strouhal number associated with vortex shedding decreases relative to the no-arc plate case.

Figure 7 presents the root mean square fluctuating pressure contours for the D-shaped cylinder with and without the arc plates. For the case without the arc plates, peak fluctuation intensity concentrates in the vicinity of the cylinder's trailing edge, coinciding with the development of the vortex shedding. The distribution of P_{rms} at R_{arc} = 0.85D remains analogous to the no-arc plate case, where the pressure fluctuations result from the interactions between the separated shear layers. At R_{arc} = 1.05D, the extended formation length and the attenuated intensity of the interactions between separated shear layers lead to the diminished P_{rms} magnitudes with the peak fluctuations shifting away from the D-shaped cylinder. The pressure fluctuations of the R_{arc} = 1.2D are enhanced near the D-shaped cylinder in comparison with R_{arc} = 1.05D due to the interactions between the shear layers once again close to the D-shaped cylinder.

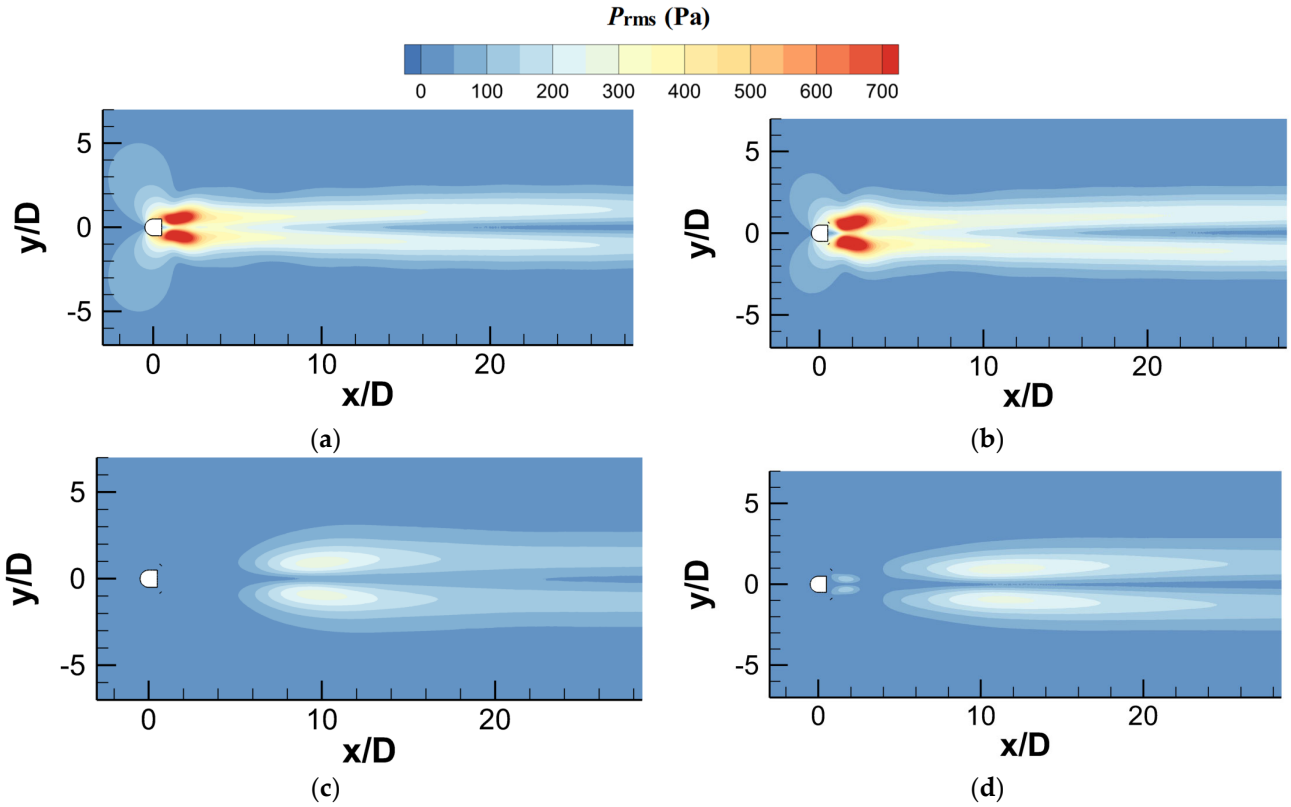

Figure 7. Root mean square fluctuating pressure contours for the D-shaped cylinder with and without the arc plates. (**a**) The no-arc plate case, (**b**) R_{arc} = 0.85D, (**c**) R_{arc} = 1.05D, and (**d**) R_{arc} = 1.2D.

The probes have been placed in the wake region as shown in Figure 1b, P1 and P2 in the near wake, and P3 and P4 further downstream of the D-shaped cylinder, to investigate the pressure fluctuations for different cases. The spectra of pressure fluctuations at these probes are shown in Figure 8. In the no-arc plate case, the interactions between detached shear flows occur in proximity to the aft section of the cylinder, resulting in substantial pressure oscillations in the wake region. With the arc splitter plates, the vortex shedding from the D-shaped cylinder is suppressed. The magnitudes of the pressure fluctuations for each probe, except P4, in the R_{arc} = 0.85D, R_{arc} = 1.05D, and R_{arc} = 1.2D cases are smaller than those of the no-arc plate case. For the no-arc plate case, the pressure spectra for the probes, P1, P2, and P4, are dominated by primary peaks with vortex shedding frequency of 0.186, which can be attributed to the effects of the significantly governed lift fluctuations on the pressure field. The spectra of P2 show the largest pressure fluctuations among the probes due to the interactions of separated shear layers near the wake. However, a main peak appears at twice the vortex shedding frequency of 0.37 in the spectra of P3 due to

the effects of the drag fluctuations on the pressure field. For R_{arc} = 0.85D, the magnitudes of the pressure spectra for P1, P2, and P3 are decreased because of the suppression of vortex shedding compared with the no-arc plate case. The spectra at P2 show the largest fluctuations among the probes. Similar with the no-arc plate case, a main peak appears at twice the vortex shedding frequency of 0.334 for P3 as a result of the effects of the drag fluctuations. However, the magnitudes of the main peaks at P4 show higher values compared with the no-arc plate case, and this is caused by the increased intensities of pressure fluctuations in the far wake due to the movement of the vortex shedding position. For R_{arc} = 1.05D, the fluctuation magnitudes reach the minimum for each probe compared with the other indicated cases, as a result of a larger degree of vorticity cancellation and the weakened interactions between the detached shear flows. The pressure spectra for each probe are dominated by primary peaks with an St of 0.114. The spectra of P4 show the largest pressure fluctuations among the probes owing to the further stretched shear layers and the vortex shedding position being further away from the D-shaped cylinder at R_{arc} = 1.05D. For R_{arc} = 1.2D, the magnitudes of the pressure fluctuations are increased in comparison with the R_{arc} = 1.05D case. As mentioned above, the flow dynamics of R_{arc} = 1.2D raise the intensities of interactions between the shear layers in comparison with R_{arc} = 1.05D, hence the pressure fluctuations. The spectra of P1 show the considerable values of pressure fluctuations due to the vortex shedding once again being close to the D-shaped cylinder. However, the spectra of P4 show the largest pressure fluctuations among the probes at R_{arc} = 1.2D. It is indicated that although the vortex shedding is once again near the alt section of the D-shaped cylinder at R_{arc} = 1.2D, the stretched shear layers separated from the outer walls of the top and bottom arc plates interact in the far wake, dominating the pressure field as well as the vortex shedding frequency.

Figures 9 and 10 present the distributions of root mean square streamwise (u'_{rms}) and transverse (v'_{rms}) velocity fluctuations for all the selected cases. The distributions of u'_{rms} and v'_{rms} in every case exhibit symmetry about the centerline of the wake, with high values observed in the wake. The intensities of velocity fluctuations in the no-arc plate case and R_{arc} = 0.85D are significantly stronger than those in the R_{arc} = 1.05D and R_{arc} = 1.2D cases due to the intense aerodynamic unsteadiness in the wake. At R_{arc} = 1.05D, the u'_{rms} and v'_{rms} magnitudes observed in the wake are considerably smaller, indicating that the arc plates suppress the flow unsteadiness in the wake. In addition, the velocity fluctuations near the D-shaped cylinder are attenuated, and the high values of u'_{rms} and v'_{rms} are mainly confined to the far wake region. In the R_{arc} = 1.2D case, the velocity fluctuations intensify again near the cylinder owing to the vortex shedding once again being close to the D-shaped cylinder compared with R_{arc} = 1.05D. In general, the wake regions display relatively low u'_{rms} and v'_{rms} levels for the cases with the arc plates, demonstrating the effectiveness of the arc splitter plates in controlling vortex shedding and flow unsteadiness.

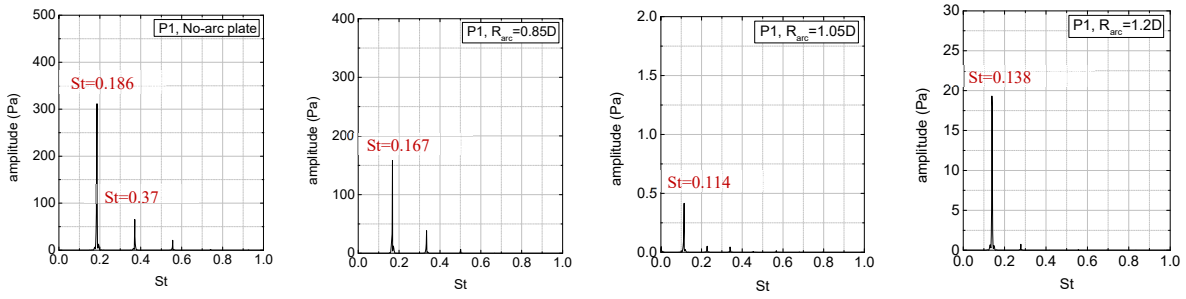

(**a**)

Figure 8. *Cont.*

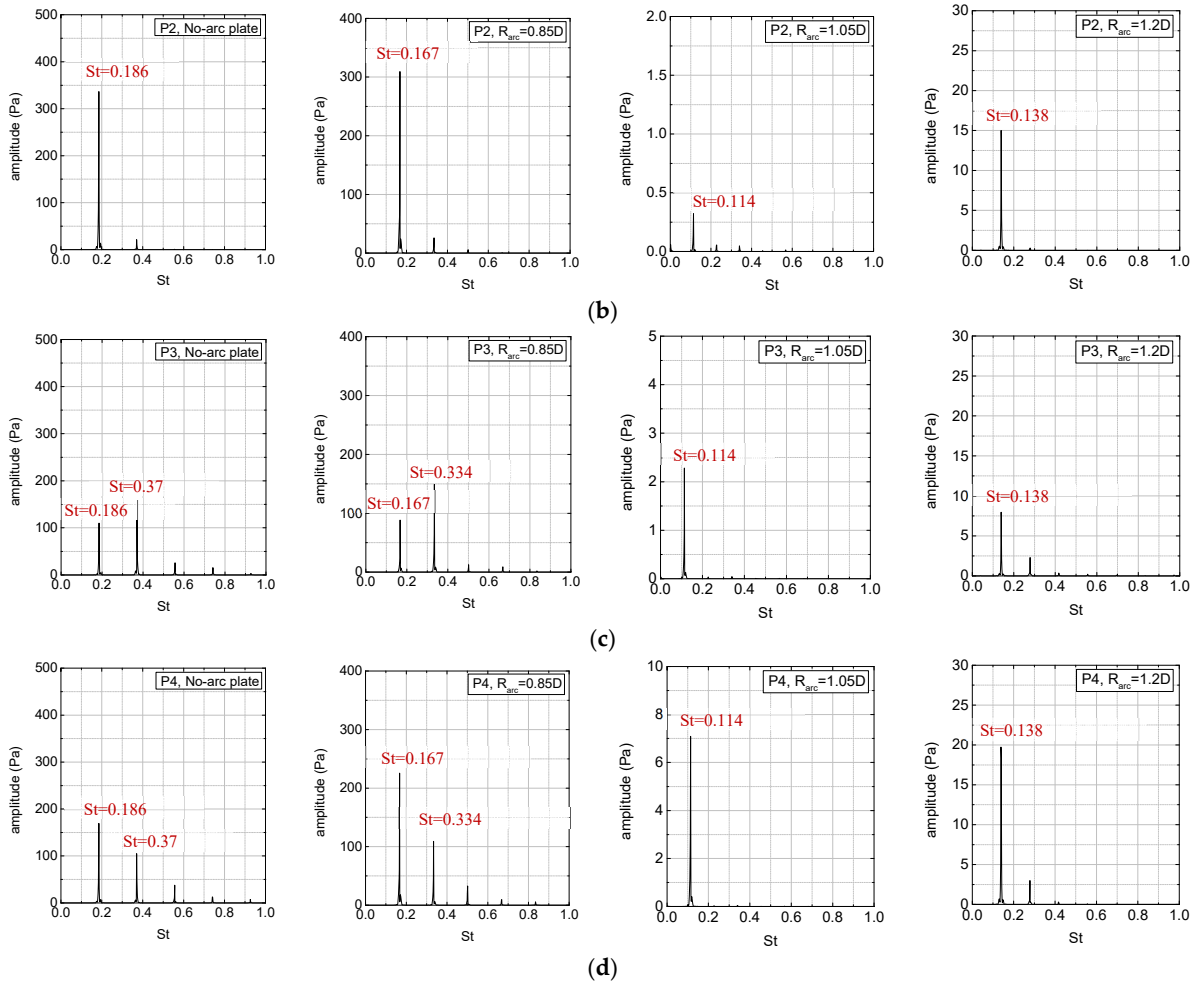

Figure 8. The spectra of the pressure fluctuations for various probes in the wake. (**a**) P1, (**b**) P2, (**c**) P3, and (**d**) P4.

The acoustic characteristics have been evaluated through the estimation of the disturbance pressure field. The disturbance pressure field can be obtained by subtracting the mean pressure from the instantaneous pressure field. Figure 11 shows the disturbance pressure contours for the cases with and without the arc plates. The disturbance pressure is non-dimensionalized by $0.5\rho U_\infty{}^2$. In the no-arc plate case, the disturbance pressure pulses originate from the upper and lower surfaces of the D-shaped cylinder owing to the alternate vortex shedding. The emitted sound exhibits pronounced directivity, with the highest intensity observed perpendicular to the flow direction. The results indicate that the lift dipole contributes more significantly to the disturbance pressure than the drag dipole for laminar flow around a D-shaped cylinder. For R_{arc} = 0.85D, a reduction in the acoustic strength is noticeable from the contours compared with the D-shaped cylinder without the arc plates. Evidently, for the R_{arc} = 1.05D and R_{arc} = 1.2D cases, the amplitudes of the radiated sound pressure are significantly reduced in comparison with the no-arc plate case. Therefore, with the introduction of the arc plates, the intensity of the radiated sound is reduced, as can be seen from the disturbance pressure contours.

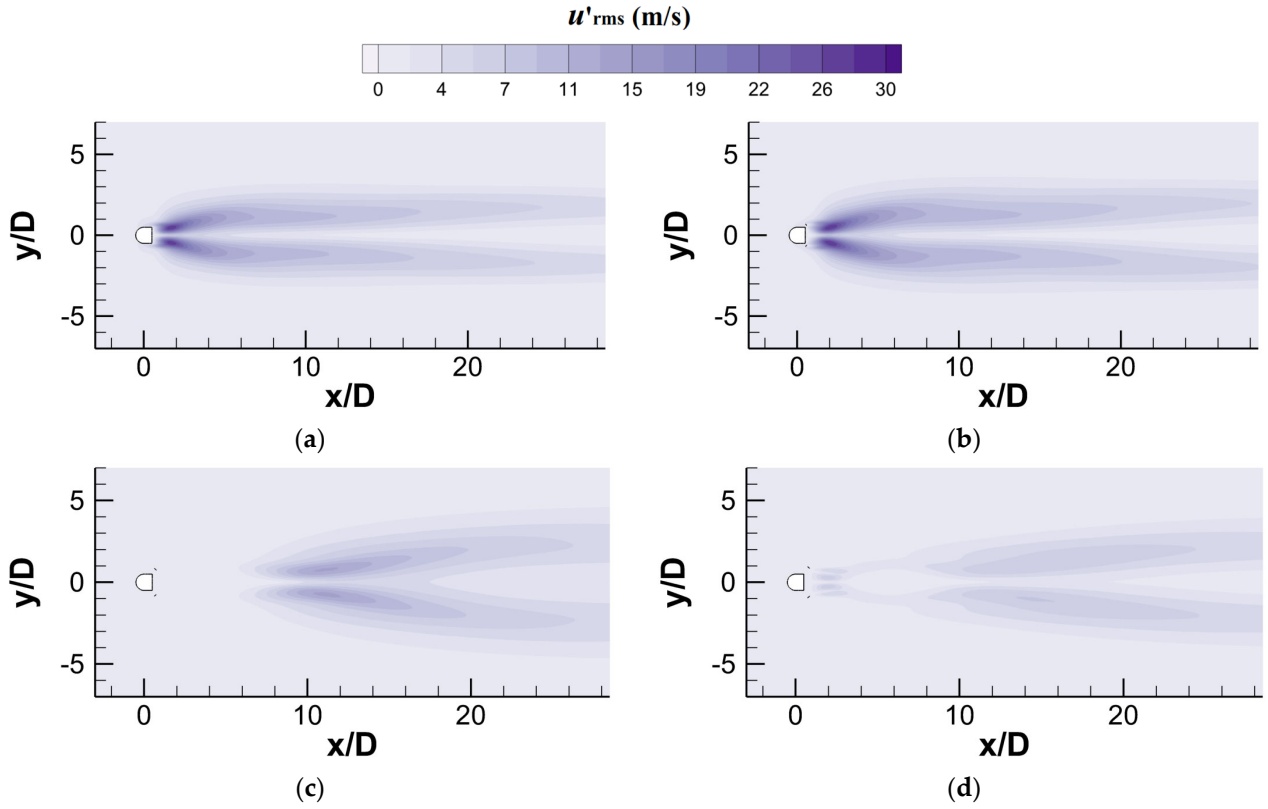

Figure 9. Distribution of velocity fluctuations u'_{rms}. (**a**) The no-arc plate case, (**b**) R_{arc}= 0.85D, (**c**) R_{arc}= 1.05D, and (**d**) R_{arc}= 1.2D.

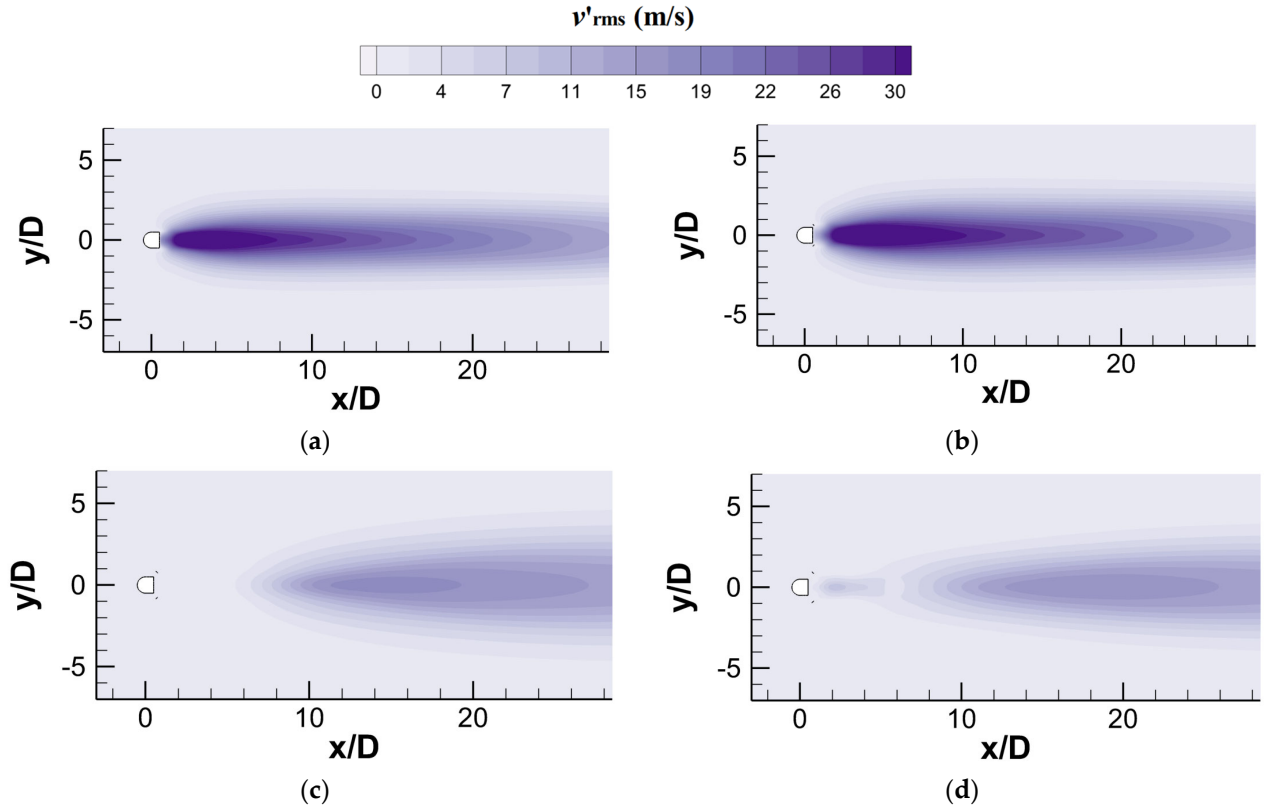

Figure 10. Distribution of velocity fluctuations v'_{rms}. (**a**) The no-arc plate case, (**b**) R_{arc} = 0.85D, (**c**) R_{arc} = 1.05D, and (**d**) R_{arc} = 1.2D.

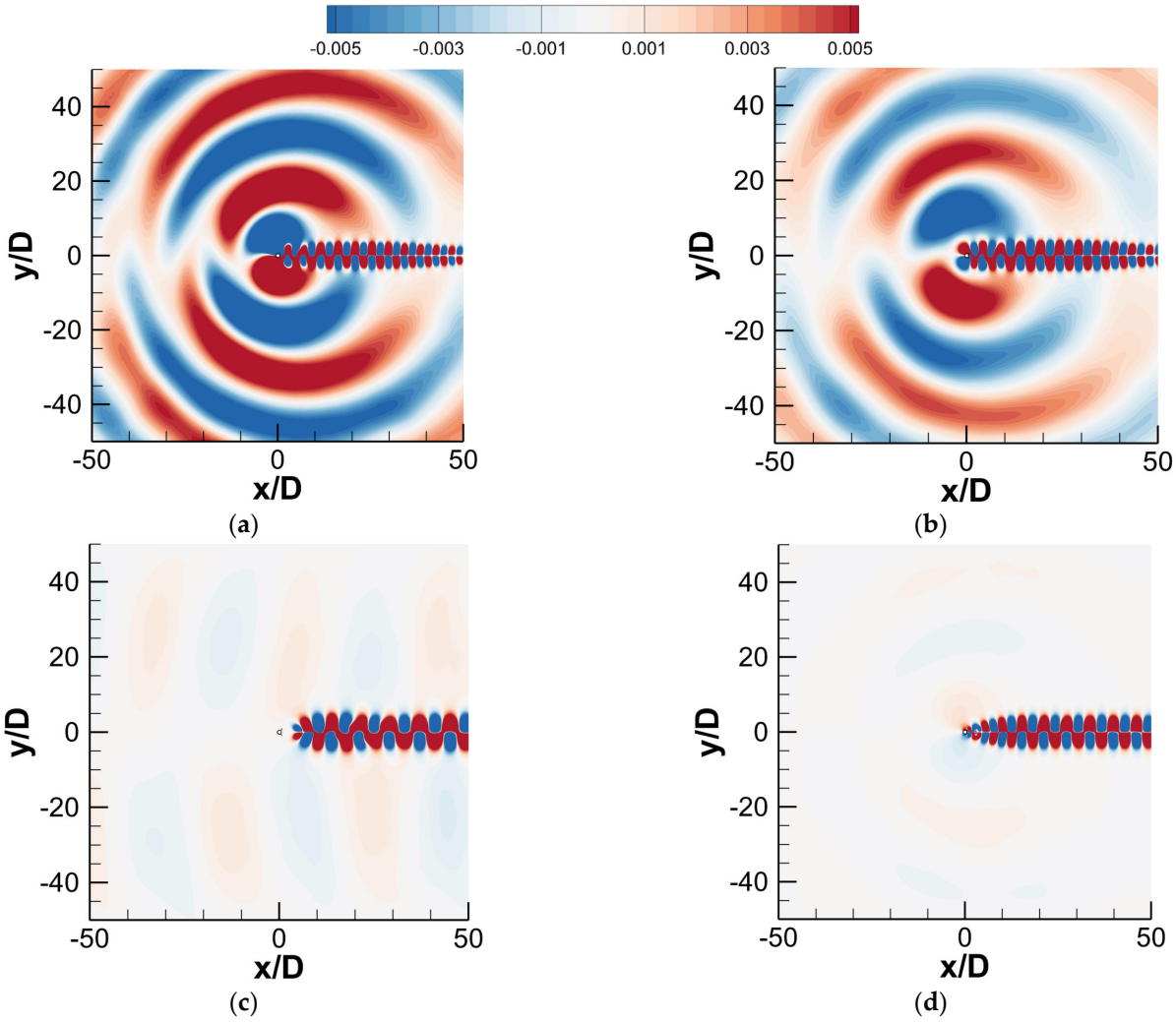

Figure 11. Contours of the disturbance pressure normalized by $0.5\rho U_\infty{}^2$ for the D-shaped cylinder with and without the arc plates. (**a**) The no-arc plate case, (**b**) R_{arc}= 0.85D, (**c**) R_{arc}= 1.05D, and (**d**) R_{arc}= 1.2D.

Figure 12 shows the time-trace sound pressure for different cases at two far-field positions, A1 (0, 150D) and A2 (150D, 0), respectively. Position A1 lies perpendicular to the free-stream direction, while A2 is situated downstream. Across all the configurations, the D-shaped cylinder without the arc plates exhibits higher amplitude of sound pressure relative to the cases with the arc splitter plates at the far-field positions. For R_{arc} = 1.05D and R_{arc} = 1.2D, the magnitudes of the acoustic pressure fluctuations are considerably lower than those in the R_{arc} = 0.85D and the no-arc plate cases. This attenuation of sound pressure fluctuations is attributed to the reduced strength of the sound source resulting from the vorticity cancellation effects and the expanded formation region of vortex shedding for R_{arc} = 1.05D and R_{arc} = 1.2D. Due to the influence of the lift fluctuations, the amplitudes of the acoustic pressure fluctuations at A1 for each case are much greater than those at A2, and the shapes of time histories of the sound pressure at A1 are similar to those of the lift coefficients.

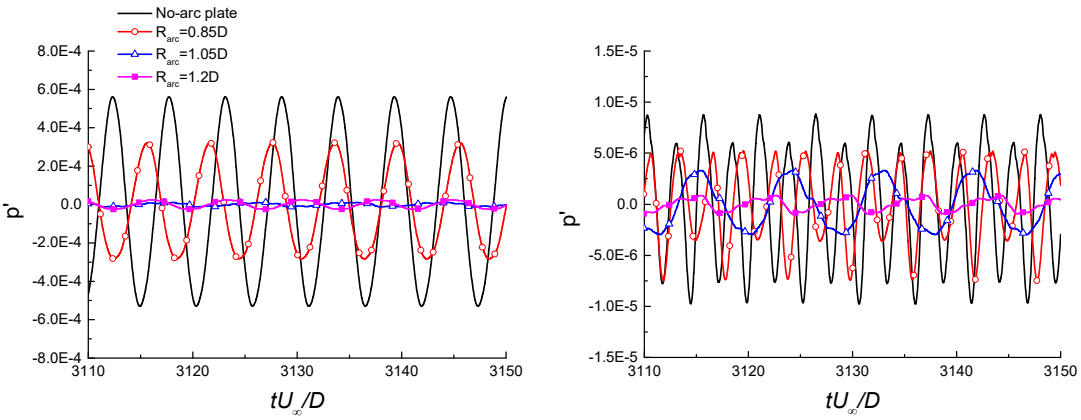

Figure 12. Time-trace sound pressure at the two far-field positions for different cases. (**a**) A1 (0, 150D) and (**b**) A2 (150D, 0).

The frequency contents of sound pressure at A1 and A2 for the cases are provided in Figure 13. The dominant peaks of the aeolian tones at A1 occur at the vortex shedding frequencies for every case, since acoustic waves propagating along the x = 0 axis are largely influenced by the lift forces. For R_{arc} = 0.85D and the case without the arc plates, the dominant peaks observed at A2 emerge at twice the vortex shedding frequency due to the fact that downstream-propagating acoustic pressure is mainly driven by the fluctuations of the drag forces, which oscillate at double the vortex shedding frequency. However, for the R_{arc} = 1.05D and R_{arc} = 1.2D cases at A2, tonal peaks are identified at the vortex shedding frequency. Obviously, the acoustic field is predominantly influenced by lift dipole sources, with a comparatively smaller contribution from drag dipoles. In every case studied, the frequencies of the aeolian tones correspond directly to the vortex-shedding frequencies and the harmonics, confirming that the acoustic emissions are synchronized with the vortex shedding process. Moreover, for the cases with the arc plates, the Strouhal number associated with vortex shedding frequency is reduced relative to the no-plate case. Consequently, the frequency of the generated acoustic pressure decreases accordingly, leading to a corresponding increase in the radiated sound wavelength.

Figure 14 presents the directivity pattern of the root mean square sound pressure at a radial distance of 150D. In the figure, the direction of the flow is from left to right. Upon the introduction of the arc plates, the results clearly show a significant effect on sound directivity. It can be found that, across nearly all directions, the cases with the arc plates consistently generate lower-amplitude acoustic waves compared to the no-arc plate case. The sound reduction is especially pronounced in the region that is approximately perpendicular to the free-stream direction. Maximum noise reduction has been noted for the R_{arc} = 1.05 cases.

In order to evaluate the impact of the arc plates on the overall sound intensity, the reduced SPL has been obtained for the cases with the arc plates. The reduced SPL is defined by:

$$SPL = 20 \log_{10} \frac{p^{rms}}{p_{ref}^{rms}} \tag{16}$$

where p^{rms} and p_{ref}^{rms} represent the root mean square acoustic pressure for the cases with and without the arc plates, respectively.

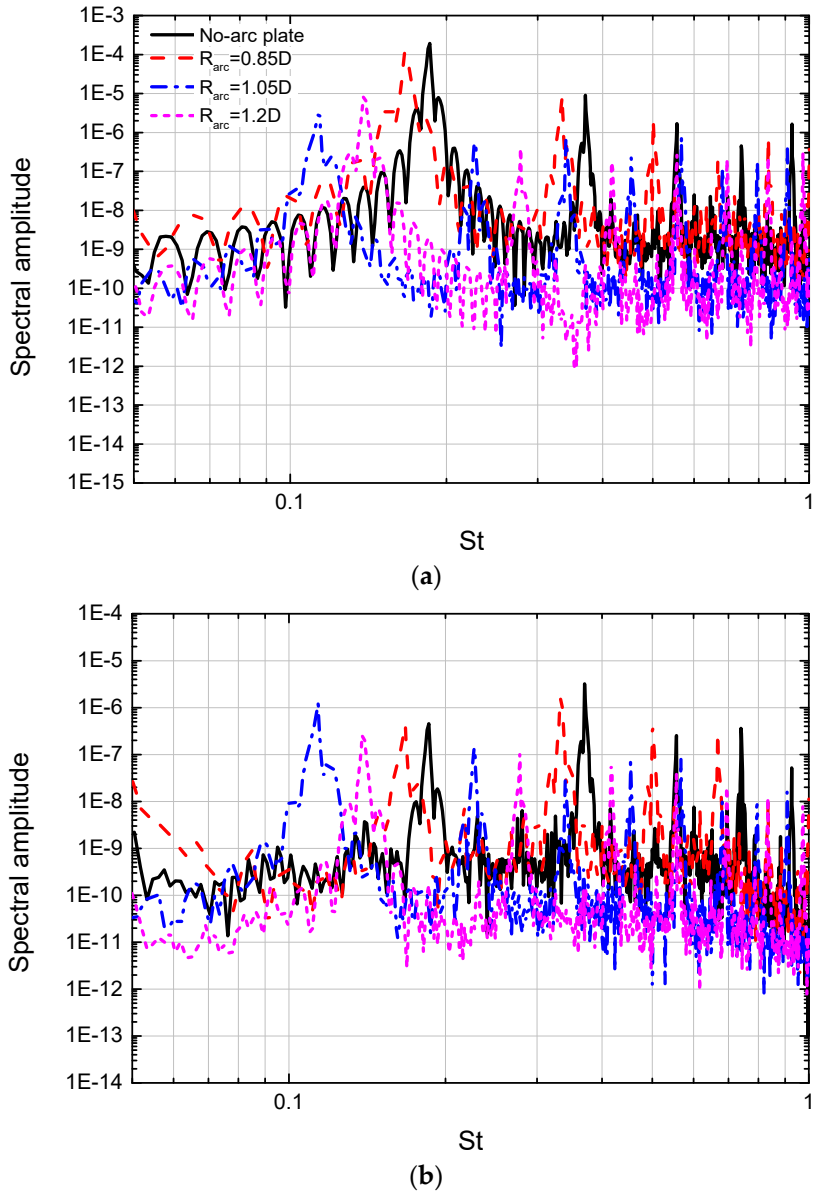

Figure 13. Frequency spectra of sound pressure at the two far-field positions for different cases. (**a**) A1 (0, 150D) and (**b**) A2 (150D, 0).

Figure 15 shows the reduced SPL for different cases at the two far-field positions, A1 (0, 150D) and A2 (150D, 0), respectively. The results of the D-shaped cylinder case without the arc plates are illustrated for reference. For the R_{arc} = 0.85D, the SPL is reduced at the two far-field positions as a result of the vortex shedding suppression. As the arc plates are positioned at R_{arc} = 1.05D, a significant reduction in aerodynamic sound at the two far-field positions is observed because of the considerable degree of vorticity cancellation. The application of the arc plates for R_{arc} = 1.05D exhibits a very effective control of sound, reducing the sound pressure level by approximately 34 dB at A1. For a larger radial distance of R_{arc} = 1.2D, the SPL is increased compared with R_{arc} = 1.05D at A1, while the SPL at A2 is smaller relative to that of R_{arc} = 1.05D. In all the cases with the arc splitter plates, the SPL values are smaller compared with the D-shaped cylinder case. As mentioned above, the implementation of the arc plates mitigates the pressure and velocity fluctuations. Thus, aerodynamic sound is decreased compared with that of the no-arc plate case.

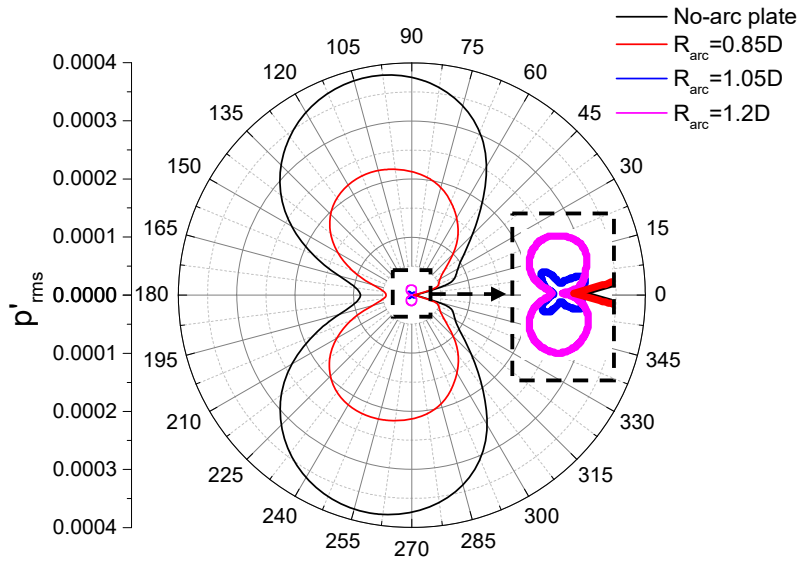

Figure 14. Directivity plots of root mean square sound pressure for the D-shaped cylinder with and without the arc plates.

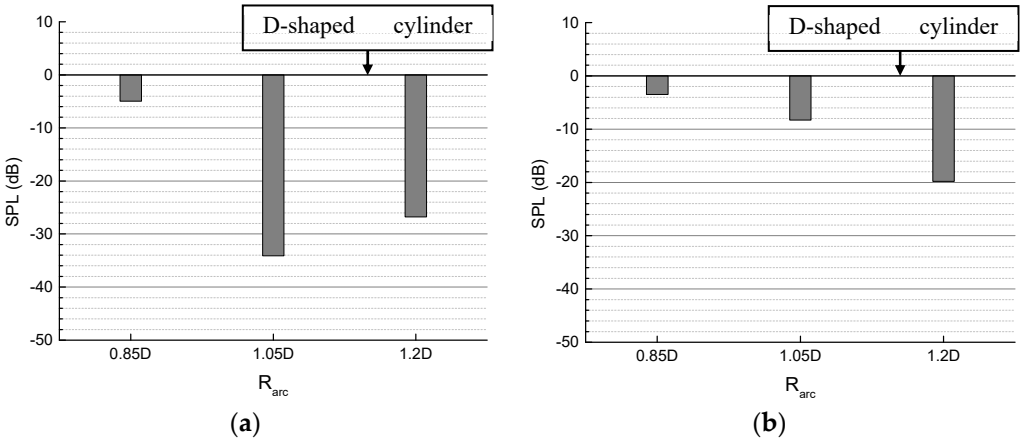

Figure 15. The reduced SPL at the two far-field positions for different cases. (**a**) A1 (0, 150D) and (**b**) A2 (150D, 0).

3.2. Effects of the Arc Angle of the Arc-Shaped Splitter Plates on the Flow and Sound

Figure 16 depicts the time-trace lift and drag coefficients for the arc plates with different angles. The results show that the arc angle clearly influences the lift and drag coefficients. The small arc angles fail to effectively guide and integrate the flow, resulting in the increased lift fluctuations, while the large arc angles lead to higher drag. For R_{arc} = 0.85D, the lift fluctuations at a 14° arc angle are relatively small, but the drag coefficient reaches its maximum among all cases. Conversely, the 2° arc angle exhibits pronounced lift fluctuations but lower drag compared to the other two angles. However, all three arc angles for R_{arc} = 0.85D show higher drag coefficients compared to the no-arc plate case. For R_{arc} = 1.05D, all three arc angles substantially reduce lift fluctuations, with the 8° and 14° cases achieving an extremely small level. Notably, the 14° arc angle produces the higher drag compared to the no-arc plate case, whereas the 2° and 8° arc angles yield drag values lower than that of the no-arc plate case, with the 2° arc angle achieving the minimum. For R_{arc} = 1.2D, the 8° and 14° arc angles significantly suppress lift fluctuations, while the 2° arc angle shows a slight reduction in lift fluctuations. Additionally, the drag coefficient for the 8° arc angle is lower than that for the 2° case, while the 14° configuration exhibits

a high drag coefficient. Notably, all three arc angles for R_{arc} = 1.2D result in higher drag coefficients than the no-arc plate case.

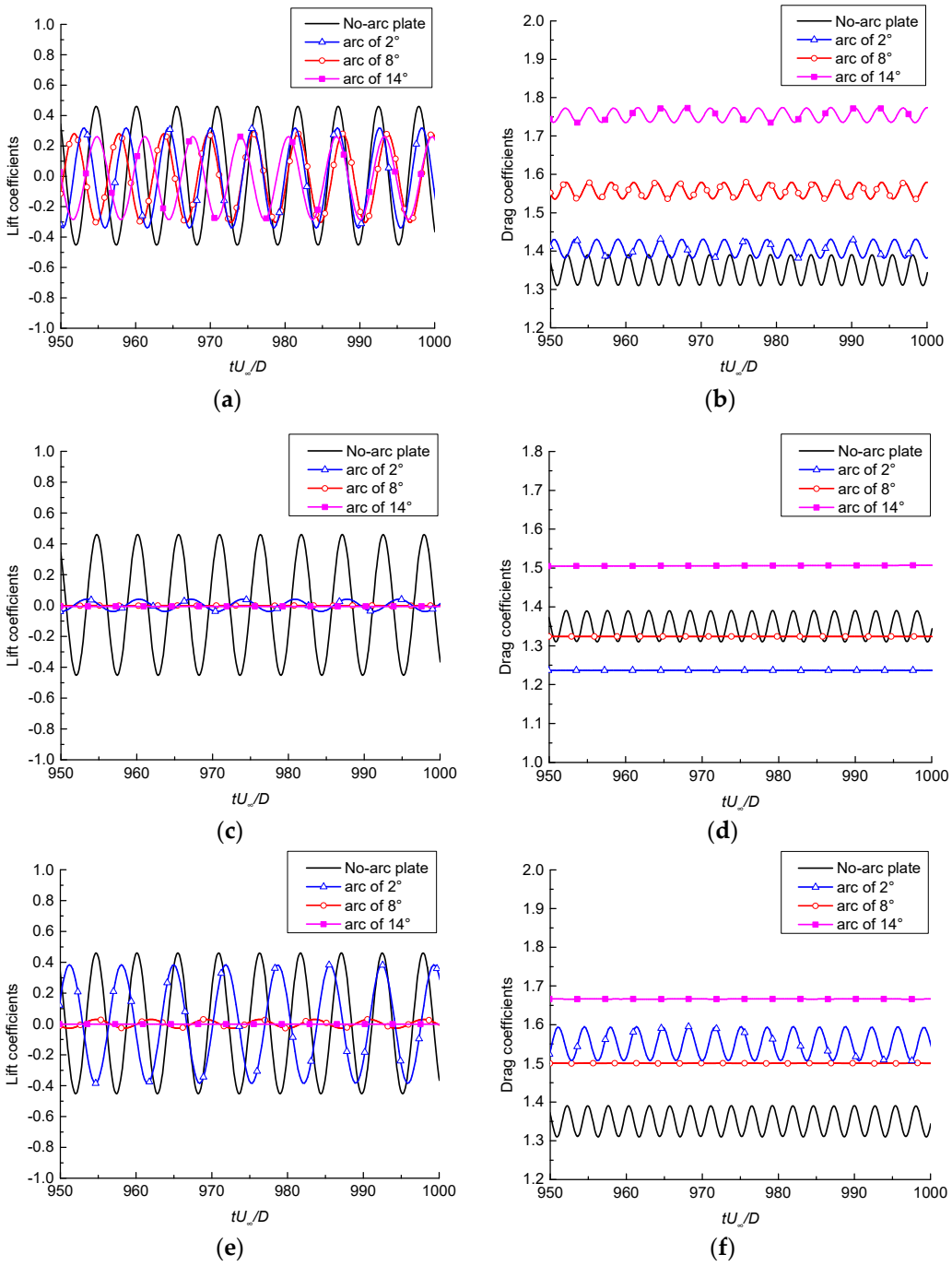

Figure 16. Time histories of lift and drag coefficients for the arc plates with different angles. (**a**,**b**) R_{arc} = 0.85D, (**c**,**d**) R_{arc} = 1.05D, and (**e**,**f**) R_{arc} = 1.2D.

Figure 17 illustrates the vorticity contours for different arc angles at R_{arc} = 1.05D, highlighting the impacts of different arc angles on the flow field. For the 2° arc angle, the vorticity cancellation of the fluid is weak, and the suppression of vortex shedding is limited. For the 8° arc angle, the vorticity cancellation is significantly enhanced, leading to a weakened Kármán vortex street. For the 14° arc angle, the vorticity cancellation further suppresses the Kármán vortex street, pushing it farther away from the cylinder. The following analysis explores the noise characteristics for different arc angles.

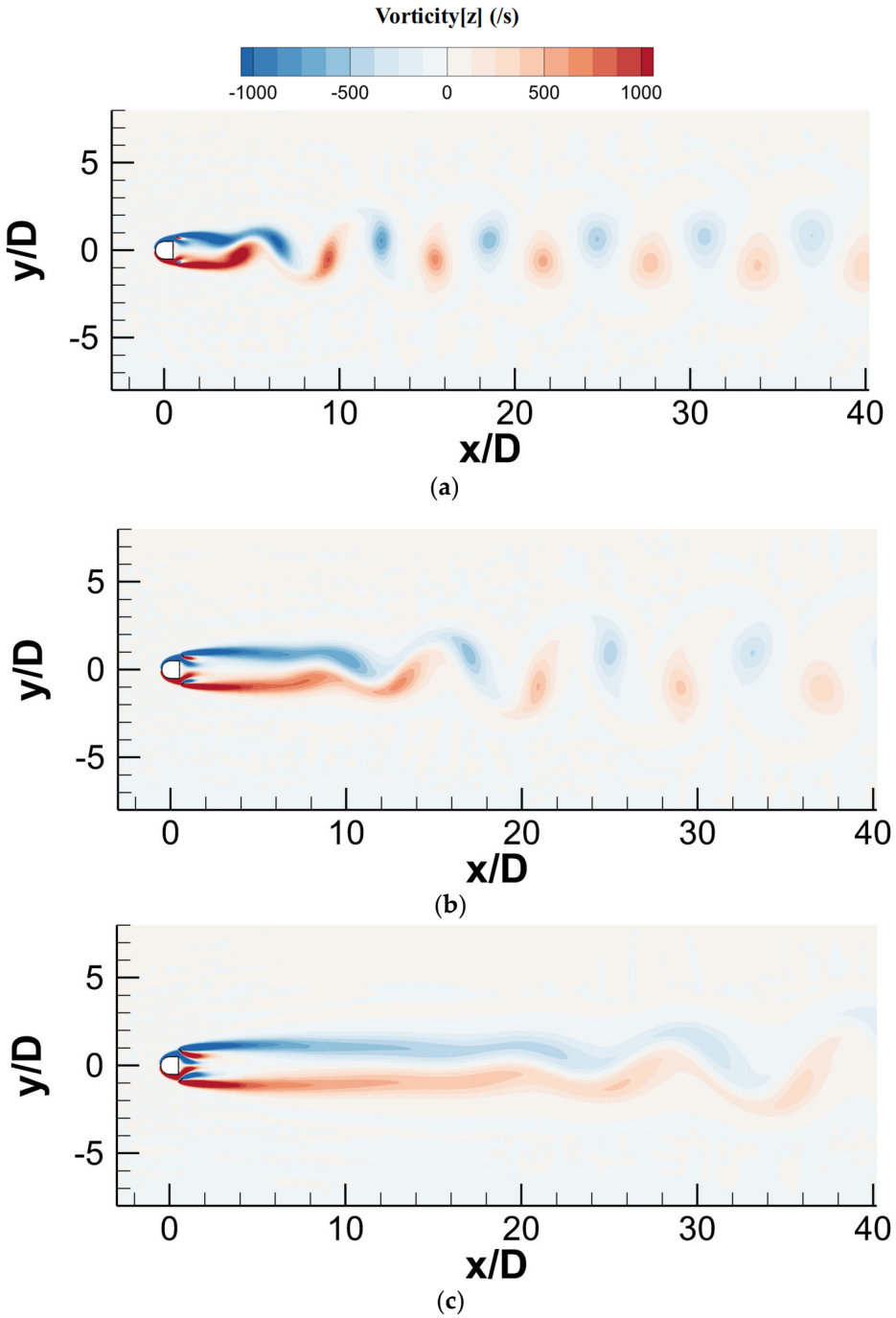

Figure 17. Instantaneous contours of vorticity z for the arc plates with different angles in the R_{arc} = 1.05D case. (**a**) 2° arc, (**b**) 8° arc, and (**c**) 14° arc.

Figure 18 shows the directivity patterns of the root mean square sound pressure at a radial distance of 150D for different cases. In the figure, the direction of the flow is from left to right. Across all the configurations, the D-shaped cylinder without the arc plates exhibits higher values of the root mean square sound pressure relative to the cases with the arc splitter plates at the far-field positions. For R_{arc} = 0.85D, the 2° arc angle produces the highest noise among all three arc angles, as the short arc fails to effectively integrate the flow. In contrast, the 14° arc angle achieves the lowest noise due to the vorticity cancellation process. However, the noise reduction is limited because the smaller radial distance (R_{arc} = 0.85D) restricts the extent of vorticity cancellation. For R_{arc} = 1.05D, all three arc angles significantly reduce noise, with the 8° arc angle yielding the minimum

noise. However, the 14° arc angle exhibits higher noise levels due to the increased noise emissions from the arc plate itself among all three arc angles. For R_{arc} = 1.2D, the 8° arc angle again achieves the lowest noise among all three arc angles, while the 14° arc angle shows relatively high noise. Among all cases analyzed, the 8° arc angle at R_{arc} = 1.05D demonstrates the most effective noise suppression.

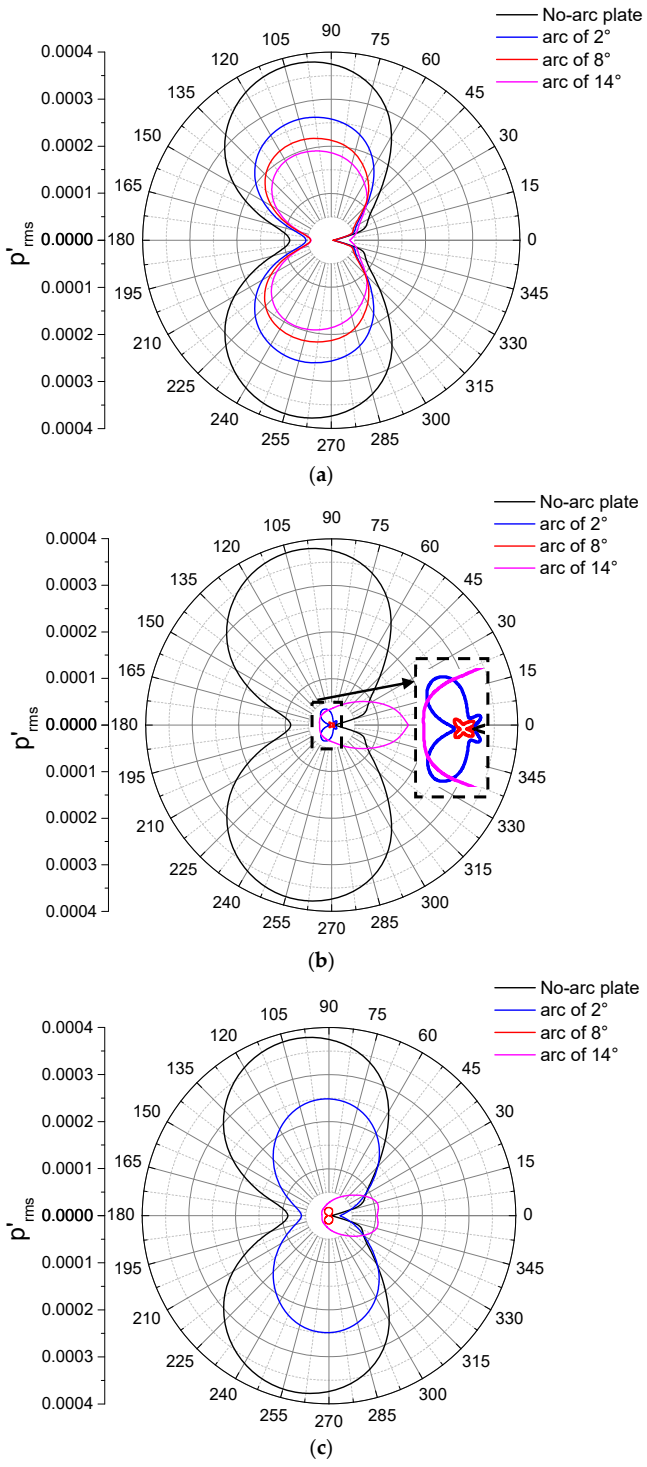

Figure 18. Directivity plots of root mean square sound pressure for the arc plates with different angles. (**a**) R_{arc} = 0.85D, (**b**) R_{arc} = 1.05D, and (**c**) R_{arc} = 1.2D.

The frequency information of sound pressure at A1 (0, 150D) for different cases is presented in Figure 19. For the different arc angles at R_{arc} = 0.85D, a reduction in the aeolian

tone at the vortex shedding frequency is observed, although the attenuation remains limited in magnitude. Additionally, the vortex shedding frequency for each arc angle shifts to lower values compared to the baseline cylinder. For R_{arc} = 1.05D, all three arc angles achieve substantial noise reduction, with the 8° arc exhibiting the most pronounced suppression of sound. For R_{arc} = 1.2D, the 8° arc again results in the lowest noise level at the vortex shedding frequency. With the 14° arc, no distinct peak corresponding to vortex shedding is evident; instead, the spectrum becomes broadband in character. For all cases with the arc plates, the Strouhal number associated with the vortex shedding frequency is reduced compared to the no-arc plate case.

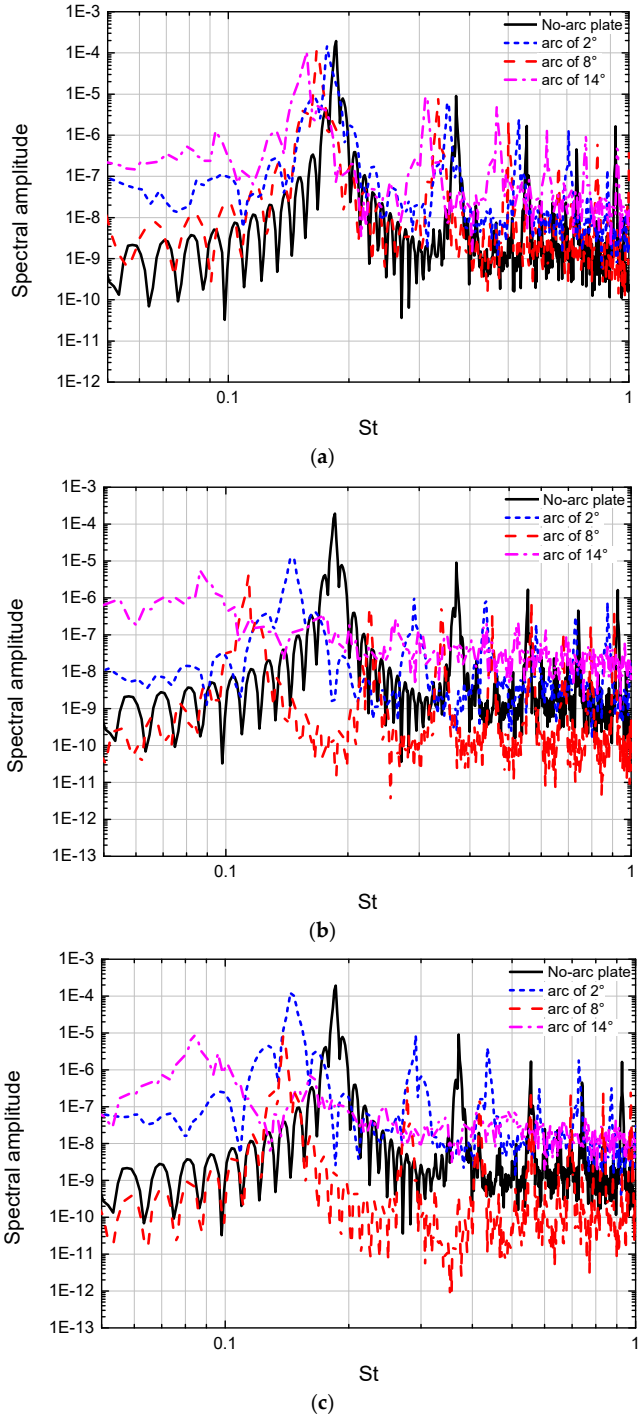

Figure 19. Frequency spectra of sound pressure at the far-field position A1(0, 150D) for different cases. (**a**) R_{arc} = 0.85D, (**b**) R_{arc} = 1.05D, and (**c**) R_{arc} = 1.2D.

4. Conclusions

In this paper, a novel assembly of arc-shaped splitter plates, which helps to reduce aerodynamic sound, has been used for a D-shaped cylinder. Flow and sound calculations have been conducted at Re = 160 to investigate the mechanism of reducing aeolian tone for the application of the arc plates. The gap between the D-shaped cylinder and the arc plates is a crucial factor since it determines the amount of fluid injected into the gap and the degree of vorticity cancellation. The arc angle of the arc plates influences the lift coefficient, drag coefficient, and noise reduction. There are significant modifications in the flow dynamics such as the flow over the D-shaped cylinder with the arc plates. The aerodynamic forces acting on the D-shaped cylinder with the arc plates exhibit lower amplitudes in both lift and drag fluctuations compared to the no-arc plate case. Due to the delayed formation of large-scale vortex shedding caused by the arc plates, the Strouhal number associated with vortex shedding decreases in comparison with the unmodified case. The vortex shedding suppression by the arc plates leads to a substantial reduction in the pressure and velocity fluctuations in the wake region.

The acoustic emissions are synchronized with vortex shedding for the D-shaped cylinder with and without the arc plates, and the frequencies of the aeolian tones correspond to the vortex-shedding frequencies and the harmonics. The SPL values at the far-field positions are reduced by the arc plates due to the vortex shedding suppression. The application of the arc plates for R_{arc} = 1.05D featuring an 8° arc shows an effective control of sound, leading to a significant reduction in SPL by almost 34 dB. This arrangement of the arc plates may be very useful to reduce the aerodynamic sound emitted from the bluff bodies.

Based on the results of this study, the arc-shaped splitter plates, as a passive control device, have the potential for applications in D-shaped or bluff structural elements subjected to steady cross-flow. This potential spans multiple engineering fields. In wind engineering, it could be applied to mitigate wind-induced "singing" or howling noise from architectural elements, such as certain lighting poles, signage supports, or the legs of rooftop equipment enclosures, thereby improving acoustic comfort in urban environments. Within transportation, the device presents a solution for reducing aerodynamic noise from exposed, non-streamlined components on high-speed trains or automotive parts, where the curved geometry of the arc plates may allow for better aerodynamic integration compared to a straight splitter. For industrial applications like heat exchangers and pipelines, where flow across tube banks generates significant noise, the arc-shaped plates offer a compact passive control method that could be integrated into tube bundles without substantially increasing the system's footprint. In aerospace applications, the fundamental principles offer potential for mitigating aerodynamic noise from bluff-body landing gear components during aircraft approach and landing, thereby addressing community noise exposure through the passive control strategy.

However, it is important to acknowledge the following limitations that may constrain the generalizability of the research findings for noise reduction in engineering problems. First of all, the current simulations are conducted in the laminar flow regime at a low Reynolds number. Most real-world applications involve turbulent flows, where the broadband disturbances could alter the noise control mechanism and effectiveness of the arc plates. Additionally, the two-dimensional model cannot capture essential 3D effects like spanwise instabilities and vortex breakdown. Finally, a uniform, steady inflow has been used in the current study, unlike realistic environments that often feature turbulent, sheared, or unsteady incoming flow. Thus, the value of this study lies in providing preliminary mechanistic insights for a novel passive flow control device. While the effectiveness of the passive

control device may vary in practical applications, the core mechanism, which involves suppressing large-scale vortex shedding to reduce noise, remains fundamentally valid.

Author Contributions: Conceptualization, B.L. and K.J.; methodology, B.L., X.C., and W.C.; software, B.L. and Q.C.; validation, B.L. and X.C.; formal analysis, B.L. and W.C.; investigation, B.L., K.J., and G.Q.; resources, B.L., K.J., and Q.C.; data curation, B.L.; writing—original draft preparation, B.L.; writing—review and editing, B.L., W.C., and K.J.; visualization, B.L. and X.C.; supervision, K.J. and G.Q.; project administration, B.L. and K.J.; funding acquisition, K.J. All authors have read and agreed to the published version of the manuscript.

Funding: This research was funded by the Research Fund for International Scientists, grant number W2431041.

Data Availability Statement: The original contributions presented in the study are included in the article, further inquiries can be directed to the corresponding author.

Conflicts of Interest: The authors declare no conflicts of interest.

References

1. Wang, X.; Bhushan, S.; Sescu, A.; Luke, E.; Manshoor, B.; Hattori, Y. Assessment of Turbulence Models for Cylinder Flow Aeroacoustics. *Aerospace* **2024**, *11*, 707. [CrossRef]
2. Ma, R.; Liu, Z.; Zhang, G.; Doolan, C.J.; Moreau, D.J. Control of Aeolian tones from a circular cylinder using forced oscillation. *Aerosp. Sci. Technol.* **2019**, *94*, 105370. [CrossRef]
3. Chamoli, S.; Joshi, A.; Rana, S.; Bhattacharaya, S.; Gupta, A.; Ghansela, S.; Thianpong, C.; Eiamsa-ard, S. Numerical methodology to reduce the drag and control flow around a Cam-shaped cylinder integrated with backward splitter plate. *Computation* **2023**, *11*, 196. [CrossRef]
4. Ganta, N.; Mahato, B.; Bhumkar, Y.G. Prediction of the aerodynamic sound generated due to flow over a cylinder performing combined steady rotation and rotary oscillations. *J. Acoust. Soc. Am.* **2020**, *147*, 325–336. [CrossRef]
5. Nogueira, L.W.; Carmo, B.S. Numerical analysis and acoustic optimization of a detached splitter plate applied for passive cylinder wake control. *J. Braz. Soc. Mech. Sci. Eng.* **2018**, *40*, 37. [CrossRef]
6. Fujisawa, N.; Hirabayashi, K.; Yamagata, T. Aerodynamic noise reduction of circular cylinder by longitudinal grooves. *J. Wind Eng. Ind. Aerodyn.* **2020**, *199*, 104129. [CrossRef]
7. Samion, S.R.L.; Ali, M.S.M.; Abu, A.; Doolan, C.J.; Porteous, R.Z.Y. Aerodynamic sound from a square cylinder with a downstream wedge. *Aerosp. Sci. Technol.* **2016**, *53*, 85–94. [CrossRef]
8. Dai, S.; Younis, B.A.; Zhang, H.; Guo, C. Prediction of vortex shedding suppression from circular cylinders at high Reynolds number using base splitter plates. *J. Wind Eng. Ind. Aerodyn.* **2018**, *182*, 115–127. [CrossRef]
9. Mahato, B.; Ganta, N.; Bhumkar, Y.G. Effective control of aeolian tone using a pair of splitter plates. *J. Sound Vib.* **2021**, *494*, 115906. [CrossRef]
10. Luo, B.; Chu, W.; Zhang, H.; Chi, Z. Control of aerodynamic sound from a circular cylinder using a splitter plate. *Mod. Phys. Lett. B* **2023**, *37*, 2250201. [CrossRef]
11. Abdi, R.; Rezazadeh, N.; Abdi, M. Reduction of fluid forces and vortex shedding frequency of a circular cylinder using rigid splitter plates. *Eur. J. Comput. Mech.* **2017**, *26*, 225–244. [CrossRef]
12. Hwang, J.Y.; Yang, K.S. Drag reduction on a circular cylinder using dual detached splitter plates. *J. Wind Eng. Ind. Aerodyn.* **2007**, *95*, 551–564.
13. Qiu, Y.; Sun, Y.; Wu, Y.; Tamura, Y. Effects of splitter plates and Reynolds number on the aerodynamic loads acting on a circular cylinder. *J. Wind Eng. Ind. Aerodyn.* **2014**, *127*, 40–50.
14. Ali, M.S.M.; Doolan, C.J.; Wheatley, V. The sound generated by a square cylinder with a splitter plate at low Reynolds number. *J. Sound Vib.* **2011**, *330*, 3620–3635. [CrossRef]
15. Ali, M.; Doolan, C.J.; Wheatley, V. Aeolian tones generated by a square cylinder with a detached flat plate. *AIAA J.* **2013**, *51*, 291–301. [CrossRef]
16. You, D.; Choi, H.; Choi, M.-R.; Kang, S.-H. Control of Flow-Induced Noise Behind a Circular Cylinder Using Splitter Plates. *AIAA J.* **1998**, *36*, 1961–1967.
17. Abbasi, S.; Souri, M. On the passive control of aeroacoustics noise behind a square cylinder. *J. Braz. Soc. Mech. Sci. Eng.* **2021**, *43*, 58. [CrossRef]
18. Karthik, K.; Vishnu, M.; Vengadesan, S.; Bhattacharyya, S.K. Optimization of bluff bodies for aerodynamic drag and sound reduction using CFD analysis. *J. Wind Eng. Ind. Aerodyn.* **2018**, *174*, 133–140. [CrossRef]

19. Octavianty, R.; Asai, M. Effects of short splitter plates on vortex shedding and sound generation in flow past two side-by-side square cylinders. *Exp. Fluids* **2016**, *57*, 143.
20. Yamagata, T.; Saito, N.; Fujisawa, N. Experimental numerical studies on aeolian tone from d-shaped cylinder. *Proc. Inst. Mech. Eng. Part C J. Mech. Eng. Sci.* **2018**, *232*, 4007–4018.
21. Yagmur, S.; Dogan, S.; Aksoy, M.H.; Goktepeli, I. Turbulence modeling approaches on unsteady flow structures around a semi-circular cylinder. *Ocean Eng.* **2020**, *200*, 107051. [CrossRef]
22. Bhinder, A.P.S.; Sarkar, S.; Dalal, A. Flow over and forced convection heat transfer around a semi-circular cylinder at incidence. *Int. J. Heat Mass Transf.* **2012**, *55*, 5171–5184. [CrossRef]
23. Barigou, M.; Mankad, S.; Fryer, P.J. Heat transfer in two-phase solid-liquid food flows: A review. *Food Bioprod. Process.* **1998**, *76*, 3–29. [CrossRef]
24. Ask, J.; Davidson, L. The sub-critical flow past a generic side mirror and its impact on sound generation and propagation. In Proceedings of the 12th AIAA/CEAS Aeroacoustics Conference (27th AIAA Aeroacoustics Conference), Cambridge, MA, USA, 8–10 May 2006; p. 2558.
25. Werner, M.J.; Würz, W.; Kraemer, E. Experimental investigation of tonal self-noise emission of a vehicle side mirror. *AIAA J.* **2017**, *55*, 1673–1680. [CrossRef]
26. Mimeau, C.; Cottet, G.H.; Mortazavi, I. Passive flow control around a semi-circular cylinder using porous coatings. *Int. J. Flow Control* **2014**, *6*, 43–50.
27. Lee, Y.W.; Cho, C.H.; Lee, D.J.; Lee, I.C. On the generations of whistle noise from an airfoil and a simplified side mirror. In Proceedings of the15th AIAA/CEAS Aeroacoustics Conference (30th AIAA Aeroacoustics Conference), Miami, FL, USA, 11–13 May 2009; p. 3349.
28. Thiria, B.; Cadot, O.; Beaudoin, J.F. Passive drag control of a blunt trailing edge cylinder. *J. Fluids Struct.* **2009**, *25*, 766–776. [CrossRef]
29. Ffowcs Williams, J.E.; Hawkings, D.L. Sound generation by turbulence and surfaces in arbitrary motion. *Philos. Trans. R. Soc. Lond. Ser. A Math. Phys. Sci.* **1969**, *264*, 321–342. [CrossRef]
30. Lighthill, M.J. On sound generated aerodynamically I. General theory. *Proc. R. Soc. Lond. Ser. A Math. Phys. Sci.* **1952**, *211*, 564–587. [CrossRef]
31. Farassat, F. *Derivation of Formulations 1 and 1A of Farassat*; Technical Memorandum TM-2007-214853; NASA: Washington, DC, USA, 2007.
32. Brentner, K.S.; Farassat, F. Analytical comparison of the acoustic analogy and Kirchhoff formulation for moving surfaces. *AIAA J.* **1998**, *36*, 1379–1386. [CrossRef]
33. Soumya, S.; Prakash, K.A. Effect of splitter plate on passive control and drag reduction for fluid flow past an elliptic cylinder. *Ocean Eng.* **2017**, *141*, 351–374. [CrossRef]
34. Park, J.; Kwon, K.; Choi, H. Numerical solutions of flow past a circular cylinder at Reynolds numbers up to 160. *KSME Int. J.* **1998**, *12*, 1200–1205. [CrossRef]
35. Yoon, H.S.; Lee, J.B.; Seo, J.H.; Park, H.S. Characteristics for flow and heat transfer around a circular cylinder near a moving wall in wide range of low Reynolds number. *Int. J. Heat Mass Transf.* **2010**, *53*, 5111–5120. [CrossRef]
36. Williamson, C.H. Oblique and parallel modes of vortex shedding in the wake of a circular cylinder at low Reynolds numbers. *J. Fluid Mech.* **1989**, *206*, 579–627. [CrossRef]
37. Buntine, J.D.; Pullin, D.I. Merger and cancellation of strained vortices. *J. Fluid Mech.* **1989**, *205*, 263–295. [CrossRef]
38. Schaffer, A. A study of vortex cancellation. *J. Aerosp. Sci.* **1960**, *27*, 193–196. [CrossRef]

Disclaimer/Publisher's Note: The statements, opinions and data contained in all publications are solely those of the individual author(s) and contributor(s) and not of MDPI and/or the editor(s). MDPI and/or the editor(s) disclaim responsibility for any injury to people or property resulting from any ideas, methods, instructions or products referred to in the content.